

## Two-Step Numerical Approach to Predict Ferrofluid Droplet Generation and Manipulation inside Multi-Laminar Flow Chambers

Jenifer Gomez-Pastora, Venos Amiri Roodan, Ioannis H Karampelas, Ali Q. Alorabi, Mark D. Tarn, Alexander Iles, Eugenio Bringas, Vesselin N. Paunov, Nicole Pamme, Edward P. Furlani, and Inmaculada Ortiz

*J. Phys. Chem. C*, **Just Accepted Manuscript** • DOI: 10.1021/acs.jpcc.9b01393 • Publication Date (Web): 01 Apr 2019

Downloaded from <http://pubs.acs.org> on April 9, 2019

### Just Accepted

“Just Accepted” manuscripts have been peer-reviewed and accepted for publication. They are posted online prior to technical editing, formatting for publication and author proofing. The American Chemical Society provides “Just Accepted” as a service to the research community to expedite the dissemination of scientific material as soon as possible after acceptance. “Just Accepted” manuscripts appear in full in PDF format accompanied by an HTML abstract. “Just Accepted” manuscripts have been fully peer reviewed, but should not be considered the official version of record. They are citable by the Digital Object Identifier (DOI®). “Just Accepted” is an optional service offered to authors. Therefore, the “Just Accepted” Web site may not include all articles that will be published in the journal. After a manuscript is technically edited and formatted, it will be removed from the “Just Accepted” Web site and published as an ASAP article. Note that technical editing may introduce minor changes to the manuscript text and/or graphics which could affect content, and all legal disclaimers and ethical guidelines that apply to the journal pertain. ACS cannot be held responsible for errors or consequences arising from the use of information contained in these “Just Accepted” manuscripts.

This document is the Accepted Manuscript version of a Published Work that appeared in final form in *Journal of Physical Chemistry C*, copyright © American Chemical Society after peer review and technical editing by the publisher.

To access the final edited and published work see <https://doi.org/10.1021/acs.jpcc.9b01393>

1  
2  
3 **Two-Step Numerical Approach to Predict Ferrofluid Droplet**  
4  
5  
6 **Generation and Manipulation inside Multi-Laminar Flow Chambers**  
7  
8  
9

10  
11 Jenifer Gómez-Pastora<sup>1,a,\*</sup>, Venos Amiri Roodan<sup>2</sup>, Ioannis H. Karamelas<sup>2,3</sup>, Ali Q.  
12  
13 Alorabi<sup>4,b</sup>, Mark D. Tarn<sup>4,c</sup>, Alexander Iles<sup>4</sup>, Eugenio Bringas<sup>1</sup>, Vesselin N. Paunov<sup>4</sup>,  
14  
15 Nicole Pamme<sup>4</sup>, Edward P. Furlani<sup>2,5,†</sup> and Inmaculada Ortiz<sup>1</sup>  
16  
17  
18  
19  
20  
21

22 1. Department of Chemical and Biomolecular Engineering, ETSIT, University of Cantabria, Avda. Los  
23  
24 Castros s/n, 39005 Santander, Spain  
25

26 2. Department of Chemical and Biological Engineering, University at Buffalo (SUNY), Buffalo, New York,  
27  
28 14260, USA  
29

30 3. Flow Science Inc., Santa Fe, New Mexico, USA  
31

32 4. Department of Chemistry and Biochemistry, University of Hull, Cottingham Road, Hull, HU6 7RX, UK  
33

34 5. Department of Electrical Engineering, University at Buffalo (SUNY), Buffalo, New York, 14260, USA  
35

36 † Deceased  
37

38 <sup>a</sup> Current address: Department of Chemical and Biomolecular Engineering, The Ohio State University,  
39  
40 Columbus, Ohio, 43210, USA  
41

42 <sup>b</sup> Current address: Albaha University, Prince Mohammad Bin Saud, Al Bahah 65527, Saudi Arabia.  
43

44 <sup>c</sup> Current address: School of Earth and Environment, University of Leeds, Woodhouse Lane, Leeds, LS2  
45  
46 9JT, UK.  
47  
48  
49  
50  
51

52  
53 \*Correspondence to: Dept. Chemical and Biomolecular Engineering, The Ohio State  
54  
55 University, 315 CBEC, 151 W Woodruff Ave., Columbus, OH 43210, USA  
56

57 E-mail: gomezpastora.1@osu.edu; Phone: +1 6142921284; Fax: +1 6142926404  
58  
59  
60

**ABSTRACT**

In this study, a computational fluid dynamics approach is implemented to investigate the dynamic behavior of continuous-flow droplet microfluidics. The developed approach predicts both droplet generation and manipulation in a two-step process. Firstly, droplet formation was studied in a flow-focusing junction through an Eulerian-Eulerian approach. Surface tension and wall adhesion were used in the model. The effect of the flow rates and geometrical characteristics of the device on droplet size and dispensing rate was investigated. Secondly, post-generation, droplets were treated as point-like-particles, and their deflection across a millimeter, multi-laminar flow chamber with five parallel streams was modeled using an Eulerian-Lagrangian approach, thus improving computational efficiency. Flow rates and magnet location were optimized. Our simulated droplet trajectory inside the chamber was contrasted against experimental data and good agreement was found between them. This two-step computational model enables the rational optimization of continuous-flow droplet processing and it can be readily adapted to a broad range of magnetically-enabled microfluidic applications.

## 1. INTRODUCTION

The use of droplet-based microfluidics has increased in the last decade as it enables the precise handling of minute amounts of fluid, e.g. nano- and picoliter-sized microreactors. These systems possess multiple advantages such as high interfacial areas and short diffusion distances which facilitate mass and heat transfer at the microscale. Moreover, they are compatible with many chemical and biological reagents, are also capable of performing a variety of “digital fluidic” operations that can be rendered programmable and the repeatability of operations can be achieved.<sup>1</sup> This not only allows the miniaturization and integration of existing chemical and biomedical protocols, but also paves the way for the development of completely new strategies for research in multiple areas.<sup>2</sup>

In order to facilitate the implementation of this technology, the precise generation and manipulation of these small vessels should be exploited. Droplet actuation in digital microfluidics is usually obtained by electrical potentials, *i.e.* “electrowetting on dielectric technology” (EWOD). This involves the application of an electrical potential to an array of electrodes patterned on a hydrophobic surface that causes variation in surface wettability.<sup>2</sup> Other actuation mechanisms have been reported as well for digital microfluidics like the magnetic and the surface acoustic wave (SAW) technologies.<sup>3,4</sup>

In contrast, droplet microfluidics or emulsion microfluidics employ specific channel geometries (T-junctions and flow-focusing junctions) to generate the droplet emulsions that are then transported in a pressure-driven flow. This approach presents multiple advantages due to its simplicity, ease of channel fabrication and high throughput.<sup>2</sup> Once the droplets are generated in a pressure-driven flow, different strategies have been implemented in order to guide the droplet trajectory within continuous-flow channels. For example, SAW technology has been used in microfluidics for generating an acoustic

1  
2  
3 radiation force on droplets with multiple applications such as mixing, separation and  
4 droplet sorting, but this technology suffers from the limitation that a high performance  
5 piezoelectric substrate can be expensive.<sup>5</sup> Dielectrophoresis has been also applied but  
6 suffers from similar limitations since a complex electrical system is required.<sup>6,7</sup> Other  
7 methods such as optical and mechanical have been reported,<sup>6</sup> but these require complex  
8 channel configurations and additional expensive, high precision, peripheral equipment  
9 (e.g. lasers). On the other hand, magnetic techniques can be considered as the most useful  
10 and elegant method for manipulating droplets inside continuous, pressure-driven flows.  
11 Droplet-based magnetic separation techniques in continuous microfluidic devices were  
12 originally proposed in 2010 by Pamme *et al.* and Lombardi *et al.*<sup>2,8,9</sup> The main advantage  
13 of this actuation method is that it does not require complex and costly channel fabrication  
14 methods and it does not require an external power source when permanent magnets are  
15 employed. This is not only an important consideration for point-of-care applications in  
16 resource-limited environments (where electricity is scarce) but it is of paramount  
17 importance for applications in life sciences, in which the interaction between the  
18 biological samples and the actuation force is a major problem.<sup>10</sup> Furthermore, this  
19 actuation method is not affected by surface charges, pH level, ionic concentration or  
20 temperature.<sup>11</sup> Moreover, different magnetic materials can be used as support for the  
21 separation. In fact, it does not strictly require the use of particles (either ferromagnetic,  
22 paramagnetic or superparamagnetic) as ionic droplets (*i.e.* droplets with dissolved  
23 paramagnetic salts) or diamagnetic droplets manipulated from magnetic fluids (*i.e.*  
24 negative magnetophoresis where the continuous phase is a ferrofluid) have recently been  
25 reported as well.<sup>12-14</sup> Nonetheless, the use of magnetic supports inside the droplet volume  
26 is beneficial as they may act as magnetic stirrers to improve the mixing of the droplet  
27 content which will improve the system performance for several applications.<sup>2</sup>  
28  
29  
30  
31  
32  
33  
34  
35  
36  
37  
38  
39  
40  
41  
42  
43  
44  
45  
46  
47  
48  
49  
50  
51  
52  
53  
54  
55  
56  
57  
58  
59  
60

1  
2  
3 With the maturity of this platform technology, sophisticated and delicate control of  
4 magnetic droplet generation, motion and transport across different flowing streams is  
5 needed to address increasingly complex applications. Numerical models provide a useful  
6 tool to further explain, understand and design the generation process and the behavior of  
7 ferrofluid droplets as they are deflected into different streams. Different authors have  
8 addressed the modeling of droplet generation, mostly by passive control by using  
9 different flow rates for the continuous phase (CP) and dispersed phase (DP),<sup>15,16</sup> but active  
10 ferrofluid droplet formation has been reported as well.<sup>17,18</sup> Numerical studies have also  
11 been developed for studying magnetic droplet splitting or breakup at T-junctions,<sup>19</sup>  
12 including magnetic droplet transport on a digital microfluidic platform.<sup>20</sup> Still, a  
13 significant part of numerical studies on ferrofluid droplets are devoted to the investigation  
14 of the motion and deformation of a single droplet under the influence of magnetic fields<sup>21-</sup>  
15 <sup>28</sup> or electric fields.<sup>29,30</sup> Other numerical studies have reported coalescence of two  
16 ferrofluid droplets when they are exposed to magnetic fields.<sup>31,32</sup> Although these studies  
17 are important and reflect the complexity of the problem (complex dynamic interaction of  
18 magnetic, surface tension and viscous forces), they are limited to a discrete number of  
19 droplets that are placed inside small fluidic structures, and for most of them, under  
20 uniform magnetic fields.

21  
22  
23  
24  
25  
26  
27  
28  
29  
30  
31  
32  
33  
34  
35  
36  
37  
38  
39  
40  
41  
42  
43  
44  
45  
46  
47  
48  
49  
50  
51  
52  
53  
54  
55  
56  
57  
58  
59  
60  
On the other hand, modeling big reaction chambers is a challenge due to the length scales  
involved in the problem. Reported numerical studies where droplets move and interact  
between them inside fluidic structures have required several hundreds of mesh cells  
across the diameter of each droplet in order to precisely track the droplet interface.<sup>31</sup>  
However, modeling droplet processing inside relatively large fluidic chambers with this  
mesh quality would be computationally very expensive. In fact, very few numerical  
studies have reported droplet processing inside millimeter sized fluidic channels, and

1  
2  
3 none of them have addressed droplet transport across multi-laminar flows. For instance,  
4  
5 Ray *et al.*<sup>33</sup> modeled a circular channel geometry of 1 mm in diameter and 150 mm in  
6  
7 length in order to describe ferrofluid droplet generation and coalescence due to an external  
8  
9 magnet. Although their mesh had only approximately 500 cells, the simulated results were  
10  
11 contrasted against experimental data and found to be in reasonable agreement. Varma *et*  
12  
13 *al.*<sup>34</sup> modeled droplet generation, deformation and merging in the presence of a uniform  
14  
15 magnetic field in a microfluidic channel with several millimeters in length employing a  
16  
17 mesh of 35,000 elements. Apart from these studies, and to the best of our knowledge, no  
18  
19 numerical study has yet reported the magnetic transport of ferrofluid droplets across  
20  
21 millimeter-sized reaction chambers where different fluids co-flow in parallel.  
22  
23  
24  
25  
26 Nonetheless, ferrofluid droplets have interesting applications as supports for reactions  
27  
28 and droplet manipulation in continuous flow has recently received great attention.<sup>8,35</sup>  
29  
30 Therefore, it is necessary to address this issue in order to efficiently design complex  
31  
32 processes where droplets are guided through relatively big chambers/channels.

33  
34  
35 The goal of the present study is to systematically study the dynamics of ferrofluid droplet  
36  
37 generation in an immiscible, non-magnetic Newtonian medium, and the later  
38  
39 manipulation when actuated by spatially non-uniform magnetic fields in a millimeter-  
40  
41 sized chamber. Oil-based ferrofluid and aqueous solutions worked as DP and CP,  
42  
43 respectively. First, we numerically predict the droplet size, shape and dispensing rate in  
44  
45 a flow-focusing device. For this droplet generation, the numerical model assumes the  
46  
47 ferrofluid as non-magnetic. Surface tension and wall adhesion were implemented in the  
48  
49 flow equations, while the Volume-of-Fluid (VOF) method was used to track the interface  
50  
51 between the ferrofluid and the aqueous CP. The simulated results were compared with  
52  
53 experimental data in order to validate the generation model. After droplet generation, their  
54  
55 manipulation in a millimeter reaction chamber was numerically predicted. For this model,  
56  
57  
58  
59  
60

1  
2  
3 analytical expressions for calculating the magnetic force acting on the droplets were  
4 implemented in the model whereas the droplets were treated as Lagrangian particles, with  
5 no volume. The advantage of this model in comparison to previous works is the reduced  
6 computational cost since we are not tracking the ferrofluid interface across a millimeter-  
7 sized chamber. Both experimental and simulation results display the same droplet  
8 trajectory along the multi-laminar flow chamber. Also, detailed hydrodynamic analysis  
9 during both formation and deflection was carried out, including the deformation of multi-  
10 laminar flow depending on the applied magnetic force, a key distinguishing feature of  
11 this work. Moreover, we demonstrate for the first time that a full modeling approach  
12 including surface tension contributions can be avoided to simulate the magnetophoretic  
13 transport in relatively large devices, thus improving computational efficiency.  
14  
15  
16  
17  
18  
19  
20  
21  
22  
23  
24  
25  
26  
27  
28  
29

## 30 **2. COMPUTATIONAL MODEL**

### 31 **2.1. Modeling approach**

32  
33 Our study begins with the generation of droplets in a flow focusing device. The theoretical  
34 description of the generation, which is important to calculate the effect of the flow rate  
35 ratio and the geometrical characteristics of the flow focusing generation device on the  
36 droplet size and dispensing rate, is described in the first subsection. The second subsection  
37 describes the magnetically induced transport of ferrofluid droplets treated as point-like  
38 particles with a fixed volume derived from the generation studies. Their motion was  
39 calculated as a balance between fluidic and magnetic forces when rectangular permanent  
40 magnets are used for droplet actuation.  
41  
42  
43  
44  
45  
46  
47  
48  
49  
50  
51  
52

53 The model was developed by customizing a commercial multiphysics Computational  
54 Fluid Dynamics (CFD) software package, *FLOW-3D* from Flow Science Inc. (version  
55 11.2, [www.flow3d.com](http://www.flow3d.com)). Specifically, custom magnetic field and force algorithms were  
56  
57  
58  
59  
60

integrated into the program to predict the field distribution from various field sources and the resulting force on the ferrofluid droplets.

## 2.2. Droplet generation

In this subsection we describe the CFD approach employed to study ferrofluid droplet generation. The main challenge in modeling multiphase systems is describing the interface movement.<sup>17</sup> There are different techniques to predict the interface location, being the most popular ones the level set (LS) and VOF methods.<sup>15,17,31</sup> In the LS method, the interface is the zero contour of a smooth function; it allows precise computation of the interface geometrical properties (*i.e.* its normal and curvature), however, the volume conservation is poor.<sup>36</sup> In this work, we employ the VOF method to calculate interface location at every time step through a phase function that describes which fluid occupies each computational cell. Although this method may lead to inaccurate curvature estimates, it naturally conserves volume accurately.<sup>36,37</sup>

Fluid configurations are defined in terms of a VOF function,  $F$ , which satisfies the following equation:<sup>38</sup>

$$\frac{\partial F}{\partial t} + \frac{1}{V_F} [\nabla(F\mathbf{A}\mathbf{v})] = 0 \quad (1)$$

where  $V_F$  and  $\mathbf{A}$  represent the fractional volume and fractional area open to flow for each mesh cell, and  $\mathbf{v}$  is the fluid velocity. The VOF function,  $F$ , represents the volumetric fraction of the incompressible phase 1 (oil-based ferrofluid) and the complementary region with volumetric fraction  $1-F$ , represents the volumetric fraction of a second fluid in every computational mesh cell (fluid 2, which is the aqueous CP). The specialty of this method is that it allows modeling two immiscible fluids by solving a set of momentum equations (by using a volume-fraction-weighted density ( $\rho$ ) and viscosity ( $\mu$ )) while

tracking the F function through the entire flow domain.<sup>18</sup> The fluid velocity field is governed by the mass continuity and momentum equations, which are solved under the assumption that the fluids are incompressible, *i.e.*:

$$\frac{\partial \mathbf{v}}{\partial t} + \frac{1}{V_F} (\mathbf{vA} \nabla \mathbf{v}) = -\frac{\nabla P}{\rho} + \mathbf{f} \quad (2)$$

$$\nabla \cdot (\mathbf{vA}) = 0 \quad (3)$$

where P is the pressure and  $\mathbf{f}$  represents the viscous accelerations that can be written as:

$$\mathbf{f} = \frac{1}{\rho V_F} [\mathbf{ws} + \nabla(\mathbf{A} \cdot \boldsymbol{\tau})] \quad (4)$$

where  $\mathbf{ws}$  is the wall shear stress (for mesh cells that contain a solid boundary) and  $\boldsymbol{\tau}$  is the shear stress tensor.

One of the advantages of using the fluid fraction of F is that it enables the simple identification of cells that may contain a sharp interface. Only for computational cells where a sharp interface is present ( $0 < F < 1$ ), the surface tension force is added as an equivalent pressure contribution to the right hand side of Eq. 2. These surface tension effects are calculated by defining the surface tension coefficient, a property that depends on the nature of the two phases that are in contact. Surface tension between the ferrofluid and aqueous continuous phase was determined to be approximately  $5 \text{ mN} \cdot \text{m}^{-1}$  (this value was determined in our previous work<sup>35</sup> for a CP containing a surfactant via tensiometer). On the other hand, for the calculation of wall adhesion, it is necessary to define the contact angle, *i.e.* the angle between the wall tangent and the fluid surface tangent, a property that depends on the nature of the two phases and the surface on which their interface is located. The contact angle was measured from experimental photographs with the open source program Measure 2.0 (C Thing software) reaching a value of  $140^\circ \pm 15^\circ$ . Hence, in the present model, a mean contact angle of  $140^\circ$  was specified initially.

In Figure 1, the generation device that was modeled is shown. It consists of a flow-focusing generation device and a T-shaped outlet, although it should be noted that droplet

behavior at the outlets is not considered for this study. The dimensions are 150  $\mu\text{m}$  in width for the inlets and the main channel and 100  $\mu\text{m}$  wide for the outlets. The length of the main channel is 2.5 mm. Different channel depths (i.e. 25  $\mu\text{m}$ , 30  $\mu\text{m}$  and 40  $\mu\text{m}$ ) were studied.

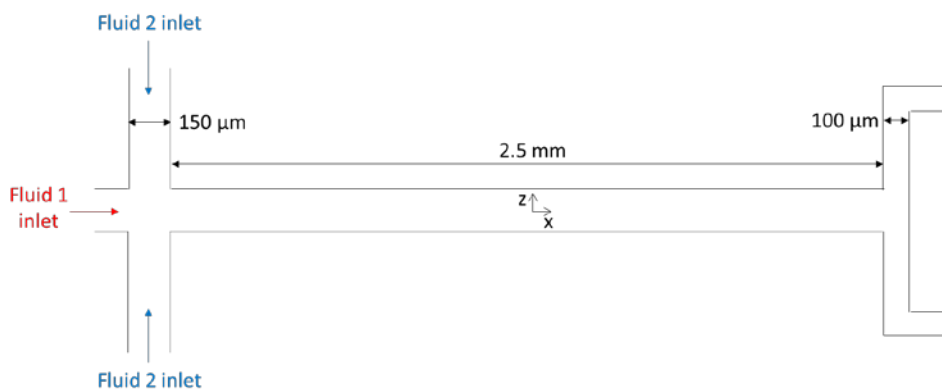


Figure 1. Schematic view of the flow-focusing droplet generation device employed in this study.

Fluid 1 represents the oil-based ferrofluid (DP), which is introduced into its inlet at a fixed flow rate of  $10 \mu\text{L}\cdot\text{h}^{-1}$ . This fluid has a density of  $1104.5 \text{ kg}\cdot\text{m}^{-3}$  and a viscosity of 4.5 cP. On the other hand, fluid 2 represents the aqueous CP, which is injected into the channel through the inlets perpendicular to the DP inlet, as seen in Figure 1. The CP fluid is modeled as water with a density and a viscosity of  $1000 \text{ kg}\cdot\text{m}^{-3}$  and 1 cP, respectively. Outflow boundary conditions were applied for the outlets and symmetry boundary conditions were applied at both limits of the y direction (i.e. 2D simulations). Finally, a uniform grid was employed for the droplet generation simulations (20,000-30,000 cells). The time step was approximately  $10^{-6}$  s for all the simulations, which took approximately 1 day to run in a multicore workstation.

### 2.3. Droplet deflection in millimeter-sized reaction chambers

After studying droplet generation in flow-focusing devices, their later manipulation inside reaction chambers when actuated by spatially non-uniform magnetic fields was addressed. In order to construct the physical model for describing the deflection across the chamber, certain assumptions and simplifications were necessary. This is due to the fact that a droplet has a deformable interface making its dynamic behavior more complicated than the magnetophoretic transport of magnetic solids. For modeling the generation, the theoretical description of the surface tension forces is necessary, as was stated in the previous section. However, for the deflection, the different length scales involved in the process make such description computationally prohibitive. As an initial test, the transport of 200  $\mu\text{m}$  ferrofluid droplets across the millimetric chamber employed in this work was modeled. The runtime of that simulation (mesh size:  $2 \cdot 10^{-5}$  m) was approximately 1 day when resolved in a modern multicore workstation and without including the magnetic force acting on the droplets. When the drop size was reduced to 100  $\mu\text{m}$ , the expected runtime increased to about 1 month (mesh size:  $10^{-5}$  m; mesh cells: 1,009,206). The increasing runtimes are due to the necessity of reducing the mesh size as the droplet size decreases in order to accurately track the interface. When trying to model magnetophoresis, the expected runtimes were assumed to be prohibitive with this fluidic domain as it would be necessary to include a subroutine that evaluates each individual mesh cell and apply the force when  $F \neq 0$  (*i.e.* in ferrofluid volumes).

Therefore, we opted for using a Lagrangian particle model for the description of droplet dynamics across the reacting chamber. The most important advantage of this model is that the droplets are now treated as discrete, point-like particles and their trajectories can be described independently of their size, although it should be noted that their size is taken as an input variable for the calculation of the forces acting on them. By treating the

1  
2  
3 droplets as discrete particles, a coarser computational mesh can be used, thereby  
4 decreasing runtimes and improving simulation efficiency. As this model employs  
5 particles of a fixed size, this information should be previously known (through the  
6 generation model developed in section 2.1).  
7  
8  
9

10  
11 For this part of our study, the Lagrangian approach is used to model droplet dynamics  
12 and the fluid transport is calculated with an Eulerian approach by solving the governing  
13 equations of fluid flow. In this study, droplets were assumed to have sizes of  
14 approximately 50  $\mu\text{m}$  and a density value of  $1104.5 \text{ kg}\cdot\text{m}^{-3}$ . These values were selected  
15 based on the properties of the DP and the flow rates employed in the experiments. The  
16 droplet deflection model was developed based on the following assumptions: (a) droplets  
17 are modeled as points and the effect of their volume into the CP displacement is neglected  
18 as well as the droplet deformation under applied magnetic fields, (b) droplets have a linear  
19 magnetization curve with saturation, (c) droplet-droplet interactions are negligible, (d)  
20 the field source is an ideal 3D rare-earth permanent magnet, and (e) there are no other  
21 magnetic materials present in the computational domain that would otherwise perturb the  
22 magnetic field. This last assumption is important as it allows for the use of analytical  
23 expressions for the magnetic field distribution and force, which greatly simplify the  
24 analysis and reduce simulation time. The aforementioned assumptions led us to  
25 simulation runtimes lower than 1 day for droplet sizes of around 50  $\mu\text{m}$ , which is an  
26 improvement with regard to conventional models.  
27  
28  
29  
30  
31  
32  
33  
34  
35  
36  
37  
38  
39  
40  
41  
42  
43  
44  
45  
46  
47

48 According to the Lagrangian approach, droplets are treated as discrete objects and their  
49 trajectories are predicted in accordance with classical Newtonian dynamics:  
50  
51

$$52 \quad m_d \frac{d\mathbf{v}_d}{dt} = \sum \mathbf{F}_{\text{ext}} \quad (5)$$

53 Here,  $m_d$  and  $\mathbf{v}_d$  are the mass and the velocity of a droplet and  $\mathbf{F}_{\text{ext}}$  represents all external  
54 force vectors exerted on it. In this work, only the dominant magnetic and fluidic forces  
55  
56  
57  
58  
59  
60

are taken into account and their formulation can be found in our previous works.<sup>39,40</sup>

Briefly, we modeled the magnetic force  $\mathbf{F}_m$  acting on a droplet using the “effective” dipole moment method in which the droplet is replaced by an “equivalent” point dipole with a moment  $\mathbf{m}_{p,eff}$  at its center as described by Furlani.<sup>41,42</sup>  $\mathbf{F}_m$  is given by:

$$\mathbf{F}_m = \mu_0 (\mathbf{m}_{p,eff} \cdot \nabla) \mathbf{H}_a \quad (6)$$

where  $\mu_0$  represents the permeability of the free space ( $4\pi \cdot 10^{-7} \text{ H} \cdot \text{m}^{-1}$ ) and  $\mathbf{H}_a$  is the applied magnetic field intensity at the center of the drop. The moment  $\mathbf{m}_{p,eff}$  can be determined using a magnetization model that takes into account self-demagnetization and magnetic saturation:

$$\mathbf{m}_{p,eff} = V_{d,m} f(H_a) \mathbf{H}_a \quad (7)$$

where the function  $f(H_a)$  is calculated as follows:

$$f(H_a) = \begin{cases} \frac{3(x_d - x_f)}{3 + (x_d - x_f)} & |H_a| < \left( \frac{(x_d - x_f) + 3}{3(x_d - x_f)} \right) M_{s,d} \\ \frac{M_{s,d}}{|H_a|} & |H_a| \geq \left( \frac{(x_d - x_f) + 3}{3(x_d - x_f)} \right) M_{s,d} \end{cases} \quad (8)$$

where  $V_{d,m}$  is the magnetic volume of a ferrofluid droplet, and  $\chi_d$  and  $M_{s,d}$  are the susceptibility and saturation magnetization. There exist different magnetization models for modeling ferrofluids with monodisperse magnetic particles. The most common one is the Langevin formulation, which is extensively employed in the specific literature.<sup>23,26,30,34</sup> However, we opted for using the model presented in Eq. 8, which has been successfully employed in the past for describing the magnetization of magnetic particles, and it is similar to other models employed in the literature for describing ferrofluids.<sup>18-20</sup> In this case, the magnetic properties of the DP ( $\chi_d = 6.79$  and  $M_{s,d} = 5.25 \cdot 10^4 \text{ A} \cdot \text{m}^{-1}$ ) were specified by the manufacturer. For this study, it is assumed that the susceptibility  $\chi_f$  of the fluid phases is essentially that of free space. The magnetic field and gradient inside the reaction chamber is provided by a Samarium Cobalt (SmCo)

1  
2  
3 rectangular magnet. This magnet has dimensions L x H x W equal to 7.3 x 4.8 x 3 mm<sup>3</sup>,  
4  
5 respectively, and a saturation magnetization of approximately 10<sup>6</sup> A·m<sup>-1</sup>. To determine  
6  
7 the 3D field distribution of the magnets, we employed an analytical model developed by  
8  
9 Furlani.<sup>43</sup>

10  
11  
12 The other dominant force acting on the droplets is the hydrodynamic force  $\mathbf{F}_{hd}$  which is  
13  
14 predicted numerically using the following expression:

$$\mathbf{F}_{hd} = -V_d \nabla P + M_{added} \left( \frac{d\mathbf{v}}{dt} - \frac{d\mathbf{v}_d}{dt} \right) + \mathbf{F}_{drag} \quad (9)$$

15  
16 where  $V_d$  is the volume of a ferrofluid droplet and  $M_{added}$  is the added mass, i.e. additional  
17  
18 resistance for an accelerating or decelerating body, which is equal to  $M_{added}=0.5\rho V_d$ .<sup>44</sup>

19  
20  $\mathbf{F}_{drag}$  is the drag force that can be obtained using a modified form of Stokes' approximation  
21  
22 for the drag on a sphere:

$$\mathbf{F}_{drag} = \frac{1}{2} \rho (\mathbf{v} - \mathbf{v}_d) |\mathbf{v} - \mathbf{v}_d| A_d C_D \quad (10)$$

23  
24 where  $A_d$  is the droplet cross sectional area.  $C_D$  is the drag coefficient for steady-state  
25  
26 flow around a sphere and can be calculated from:

$$C_D = \frac{24}{Re_p} + \frac{6}{1+\sqrt{Re_p}} + 0.4 \quad (11)$$

27  
28 where  $Re_p$  is the particle (*i.e.* droplet) Reynolds number. For droplet deflection, the fluid  
29  
30 velocity field was predicted by using the Navier Stokes and continuity equations for  
31  
32 incompressible fluids, including droplet-fluid interactions (*i.e.* a two-way coupling model  
33  
34 with momentum transfer from the droplet to the fluid and vice versa) as follows:

$$\frac{d(\rho\mathbf{v})}{dt} = -\nabla P + \text{div}(\boldsymbol{\tau}) + \frac{1}{V} \mathbf{F}_P \quad (12)$$

$$\nabla \cdot (\mathbf{v}) = 0 \quad (13)$$

35  
36 where the  $\text{div}(\boldsymbol{\tau})$  term represents the viscous accelerations and  $V$  is the volume of fluid in  
37  
38 the cell. The last term in Eq. 12 represents droplet induced fluid accelerations and  $\mathbf{F}_P$  can  
39  
40 be written as:

$$\mathbf{F}_p = -\sum \left[ \mathbf{F}_{\text{drag}} + M_{\text{added}} \left( \frac{d\mathbf{v}}{dt} - \frac{d\mathbf{v}_d}{dt} \right) \right] \quad (14)$$

Regarding the fluidic domain, Figure 2 represents the reaction chamber modeled for droplet deflection. The main chamber has dimensions of 8 x 4.1 x 0.1 mm<sup>3</sup>. It has five inlets with different widths (0.3 mm, 1 mm, 1 mm, 1 mm and 0.8 mm, for inlet 1, 2, 3, 4 and 5, respectively) through which multiple aqueous solutions can be injected, as seen in Figure 2.

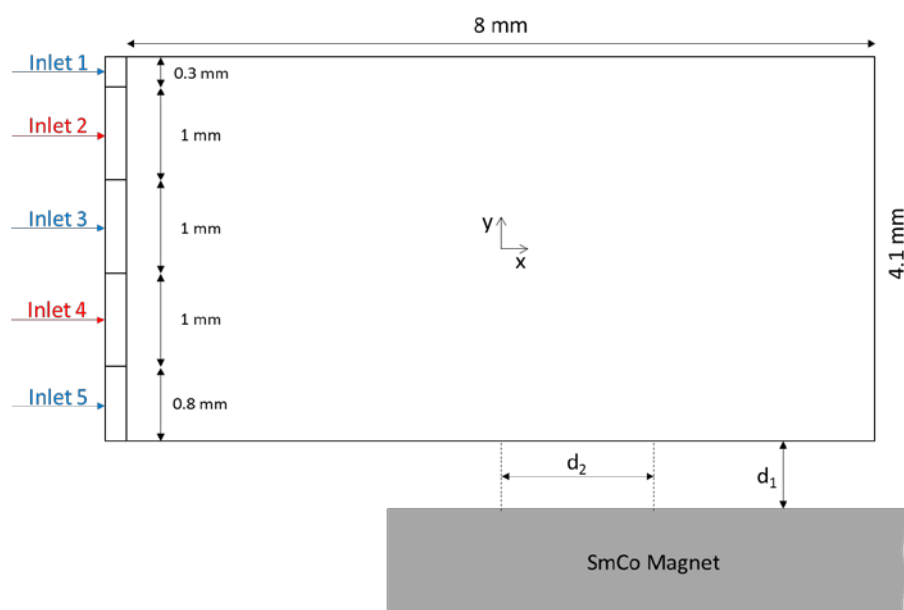


Figure 2. Schematics of the reaction chamber in which ferrofluid droplets are deflected across multi-laminar flow streams.

Droplets are injected through inlet 1 (a fixed diameter of 50  $\mu\text{m}$  was set as mentioned above) along with the aqueous CP. The dispensing rate was selected as a function of the DP and CP flow rates. Inlets 2-5 were used to inject aqueous water solutions. In order to distinguish the co-flow of the 5 laminar flows across the chamber, scalar solutes were added in streams 2 and 4, an approach useful to evaluate fluid-droplet interactions. A no-slip condition (zero velocity) is applied along the microchannel walls, and at the outlet, an outflow boundary condition is employed. Symmetry boundary conditions are applied

1  
2  
3 at both limits of the z direction (*i.e.* into the page). Although the force balance for each  
4 droplet is solved within a 3D analysis (the magnetic field distribution and magnetic force  
5 is calculated in x, y, and z directions), the governing equations for the flow along the  
6 width of the channel (z axis) are not considered. The droplet trajectory was calculated as  
7 a function of the flow rate of the streams and the magnetic field conditions inside the fluid  
8 domain (provided by different magnet positions with respect to the main chamber). The  
9 flow rates of streams 2-5 were varied, and took the values of either 300  $\mu\text{L}\cdot\text{h}^{-1}$  or 600  
10  $\mu\text{L}\cdot\text{h}^{-1}$ . The flow rate of stream 1 (CP) was varied from 150  $\mu\text{L}\cdot\text{h}^{-1}$  to 300  $\mu\text{L}\cdot\text{h}^{-1}$ . Four  
11 magnet positions were tested. For each position, the distance between the top of the  
12 magnet and the bottom of the chamber ( $d_1$ ), and the distance between the center of the  
13 magnet and the center of the chamber in x direction ( $d_2$ ), took a different value (see Figure  
14 2). Table 1 shows the value of these distances for each of the magnet positions tested.  
15  
16  
17  
18  
19  
20  
21  
22  
23  
24  
25  
26  
27  
28  
29  
30  
31  
32

33 Table 1. Magnet positions tested in this study

Magnet position	Distance $d_1$ (mm)	Distance $d_2$ (mm)
1	5.5	0
2	5.5	7.65
3	0	7.65
4	5.5	4

34  
35  
36  
37  
38  
39  
40  
41  
42  
43 Finally, a mesh independence study was carried out in order to optimize the total number  
44 of cells used in the simulations. Simulations were performed with different mesh sizes,  
45 *i.e.* the grid was progressively refined and the difference in the obtained flow patterns was  
46 calculated. Four mesh sizes were tested: i) G1:  $100\cdot 10^{-6}$  m; ii) G2:  $50\cdot 10^{-6}$  m; iii) G3:  
47  $20\cdot 10^{-6}$  m and iv) G4:  $10\cdot 10^{-6}$  m mesh sizes. It was found that a mesh refinement beyond  
48 G3 did not report an appreciable improvement of the results, and therefore, for droplet  
49 deflection simulations the mesh was composed by approximately 250,000 cells with a  
50  
51  
52  
53  
54  
55  
56  
57  
58  
59  
60

1  
2  
3 size of  $20 \cdot 10^{-6}$  m. The time step was around  $10^{-4}$ - $10^{-3}$  s for all the simulations, which took  
4  
5 less than 1 day to run in a multicore workstation.  
6

7  
8 The model was developed by customizing *FLOW-3D* (version 11.2). Custom magnetic  
9  
10 field and force algorithms were integrated into the program to predict the field distribution  
11  
12 generated by the SmCo magnet, and the corresponding magnetic force on the ferrofluid  
13  
14 droplets (with *Visual Studio* version 2013). *MatLab* version 2015 was also used for the  
15  
16 analysis of the magnetic field and magnetic force exerted on the droplets inside the  
17  
18 reaction chamber.  
19  
20

### 21 22 23 24 **3. EXPERIMENTAL METHODS**

25  
26 The model was experimentally validated by using different microdevices that were  
27  
28 fabricated in glass using conventional photolithography and wet etching techniques.<sup>45</sup> For  
29  
30 the droplet generation, experiments were performed using a glass flow focusing  
31  
32 microdevice (Figure 3 a) and b)) with a U-shaped cross-section of  $150 \mu\text{m} \times 30 \mu\text{m}$  (for  
33  
34 the inlets and main channel) and  $100 \mu\text{m} \times 30 \mu\text{m}$  (T-outlet). Two different fluid phases  
35  
36 were pumped into the two inlets. The DP was composed of an oil-based ferrofluid  
37  
38 (EMG901, Ferrotec), containing a suspension of 10 nm diameter  $\text{Fe}_3\text{O}_4$  nanoparticles at  
39  
40 a concentration of 11.8 vol%, dissolved in ciclohexane (50% v/v) (Fisher Scientific). The  
41  
42 CP was composed of an aqueous acetate buffer (pH 4, 20 mM) prepared from sodium  
43  
44 acetate (Sigma Aldrich) and acetic acid (Fisher Scientific), Tween 20 (0.5% v/v) and  
45  
46 poly(vinylpyrrolidone) ( $10 \text{ mg} \cdot \text{mL}^{-1}$ ) both purchased from Sigma Aldrich. The effect of  
47  
48 the flow rate on both droplet size and dispensing rate was investigated by keeping the DP  
49  
50 at  $10 \mu\text{L} \cdot \text{h}^{-1}$  and varying the CP from 40 to  $500 \mu\text{L} \cdot \text{h}^{-1}$ .  
51  
52  
53

54  
55 For the deflection studies, the droplets were generated in a flow focusing channel, guided  
56  
57 through a serpentine and deflected across a multi-laminar flow chamber ( $8 \text{ mm} \times 4.1 \text{ mm}$ )  
58  
59  
60

1  
2  
3 x 0.1 mm) as seen in Figure 3 c). This chip consisted of two etched glass plates that were  
4  
5 bonded together. The top plate featured a droplet generation region that consisted of a T-  
6  
7 junction and was etched to a depth of 20  $\mu\text{m}$ , while the bottom plate with the serpentine  
8  
9 and the reaction chamber was etched to a depth of 100  $\mu\text{m}$  (Figure 3 d)). This chip was  
10  
11 mounted into an aluminum chip holder designed and fabricated in-house (Figure 3 e)).  
12  
13 For the deflection studies, DP was pumped into inlet 1 at 1 or 10  $\mu\text{L}\cdot\text{h}^{-1}$ , while the aqueous  
14  
15 CP was pumped into inlet 2 at flow rates that varied from 150 to 300  $\mu\text{L}\cdot\text{h}^{-1}$ . Droplets  
16  
17 were deflected through alternating streams of red and blue inks (printer refill ink),  
18  
19 pumped into inlets 3-6 at flow rates that varied from 300 to 600  $\mu\text{L}\cdot\text{h}^{-1}$ . A 3 x 4.8 x 7.3  
20  
21  $\text{mm}^3$  SmCo (Magnet Sales, UK) was used for the generation of the magnetic field, which  
22  
23 was placed on top of the chip at different distances from the chamber. Positioning of the  
24  
25 magnets was aided by the incorporation of scale bars into the chip designs.  
26  
27  
28 Fused silica capillaries (150  $\mu\text{m}$  i.d., 375  $\mu\text{m}$  o.d., Polymicro Technologies) were glued  
29  
30 into the flow focusing device or connected to the inlet/outlet holes of the deflection chip  
31  
32 through the aluminum holder. The capillaries connected to the inlet holes of the chips  
33  
34 were connected to 500  $\mu\text{L}$  glass syringes (SGE, Sigma-Aldrich, UK) that were driven by  
35  
36 three precision syringe pumps (PHD2000, Harvard Apparatus, Biochrom, UK): one pump  
37  
38 for the DP and one pump for the CP for droplet generation, and one pump for the multiple  
39  
40 solutions pumped into the reaction chamber for processing the droplets. Droplet  
41  
42 generation and deflection was observed via an inverted fluorescence microscope (Eclipse  
43  
44 Ti, Nikon, UK) equipped with a high resolution CCD camera (Retiga EXL, Media  
45  
46 Cybernetics, UK). ImageJ freeware (<https://imagej.nih.gov/ij/>) was used for the analysis  
47  
48 of droplet size.  
49  
50  
51  
52  
53  
54  
55  
56  
57  
58  
59  
60

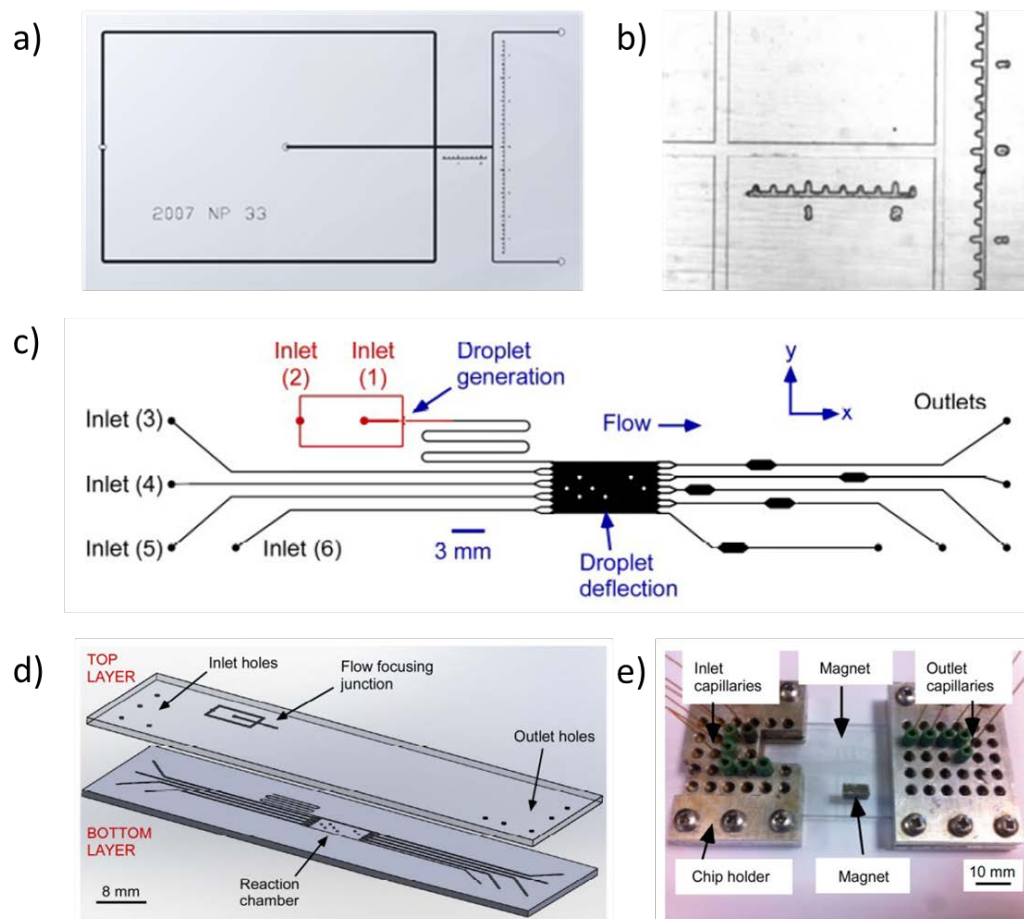


Figure 3. a) CAD design of the flow-focusing droplet generation junction employed for validating the theoretical model. b) Experimental micrograph of the section modeled (scale bars are in mm). c) Schematics of the glass chip used for the droplet deflection studies. The chip is composed of two etched plates: a top layer featuring an interchangeable droplet generation junction (20  $\mu\text{m}$  deep, shown in red in the CAD design), and a bottom layer featuring a channel structure for the magnetic deflection of droplets through reagent and washing streams (100  $\mu\text{m}$  deep). d) An exploded view of the two-part chip. e) Aluminum chip holder used to interface the glass chip to inlet and outlet capillaries. A magnet was placed at the top of the chip, below the reaction chamber.

## 4. RESULTS AND DISCUSSION

### 4.1. Droplet generation studies

The flow-focusing droplet generation device was employed first to investigate droplet formation and validate our Eulerian-Eulerian model. Oil-based ferrofluid DP was pumped into the inlet 1 at a flow rate of  $10 \mu\text{L}\cdot\text{h}^{-1}$  while an aqueous CP was pumped into inlet 2 at a range of flow rates between  $100$  and  $500 \mu\text{L}\cdot\text{h}^{-1}$ . Three chip depth values were analyzed, *i.e.*  $25$ ,  $30$  and  $40 \mu\text{m}$ . In Figure 4, the droplet generation simulation results for two of the chip depths are presented (*i.e.*  $25 \mu\text{m}$  and  $40 \mu\text{m}$  deep channels). The results for the  $30 \mu\text{m}$  deep generation device are not shown in the figure due to the small differences reported from the three geometries. As it can be seen in Figures 4 a) and b), when the value of the CP flow rate is relatively small ( $100 \mu\text{L}\cdot\text{h}^{-1}$ ), the size of the generated droplets is relatively large, *i.e.* droplet diameter varies from  $187.84 \mu\text{m}$  to  $233.21 \mu\text{m}$  depending on the chip depth. Moreover, due to the low velocity of the CP (and high residence time), the separation distance between two consecutively formed droplets is small. In Figures 4 c) and d), the velocity vectors during droplet generation are shown at the same time as in Figures 4 a) and b). As it can be perceived from the velocity contours, ferrofluid droplets are generated at the flow-focusing at a small velocity. However, once generated, they travel along the chip straight section at the same velocity as the CP phase. In Figures 4 e) and f), the droplet generation simulation results for the CP flow rate equal to  $300 \mu\text{L}\cdot\text{h}^{-1}$  are shown. In this case, droplet size decreased considerably, *i.e.* ranging from  $159.83 \mu\text{m}$  to  $173.49 \mu\text{m}$ . This reduction in droplet size is due to the large velocity values for the CP at this flow rate. When the CP flow rate was further increased to  $500 \mu\text{L}\cdot\text{h}^{-1}$ , droplet sizes were reduced to  $133.32$ - $150.32 \mu\text{m}$ , as seen in Figures 4 g) and h)). For both chips, as the CP flow rate value increases, droplet size decreases and the separation between two consecutively generated droplets increases due

to the lower residence time. Finally, as the CP flow rate increases, the difference between the droplet sizes reported for both geometries decreases, *i.e.* very similar droplet sizes are obtained for the three geometries under CP flow rates as high as  $500 \mu\text{L}\cdot\text{h}^{-1}$ . These results are in agreement with previous published works.<sup>15,16</sup>

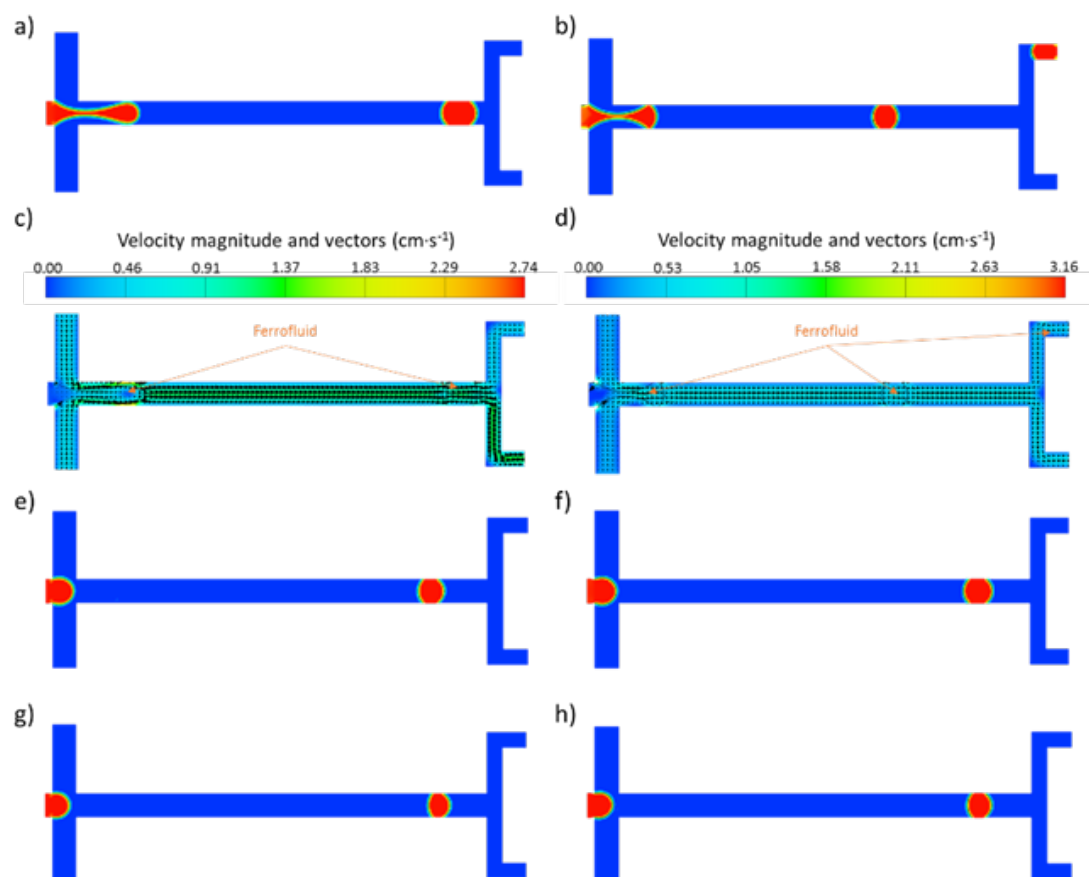


Figure 4. Droplet generation studies for different chip configurations. Droplet generation for a CP flow rate equal to  $100 \mu\text{L}\cdot\text{h}^{-1}$  for the a)  $25 \mu\text{m}$  deep and b)  $40 \mu\text{m}$  deep channel; Figures 5 c) and d) present the fluid velocity vectors at the same time as presented in Figures 5 a) and b). Figures 5 e)-h) show droplet generation for CP flow rates equal to  $300 \mu\text{L}\cdot\text{h}^{-1}$  (figures e) and f)) and equal to  $500 \mu\text{L}\cdot\text{h}^{-1}$  (figures g) and h)).

In Figure 5 a), the comparison between the theoretical droplet size as a function of the CP flow rate is presented for the three geometrical configurations. As it can be seen in the

1  
2  
3 figure, the droplet size is similar for the three geometries modeled in this study. Droplet  
4 size slightly increases (between 8% and 12% for flow rates between 200 and 500  $\mu\text{L}\cdot\text{h}^{-1}$ )  
5 as the depth of the channel increases. When the CP flow rate decreases to 100  $\mu\text{L}\cdot\text{h}^{-1}$ , the  
6 droplet size obtained with the three chips is similar, and even bigger droplets are reported  
7 for the 25  $\mu\text{m}$  deep channel. This could be due to the inhomogeneous drops obtained for  
8 these flowing conditions. As seen in the figure, the error bars are large for this flow rate  
9 condition. For this CP flow rate value, droplets bigger than 250  $\mu\text{m}$  and smaller than 200  
10  $\mu\text{m}$  are consecutively generated with each of the devices. This does not happen when the  
11 CP flow rate increases, as very homogeneous droplets are generated for these flowing  
12 conditions (see error bars in the figure for CP flow rates greater than 100  $\mu\text{L}\cdot\text{h}^{-1}$ ).  
13  
14  
15  
16  
17  
18  
19  
20  
21  
22  
23  
24  
25

26 In Figure 5 b) the dispensing rate is presented as a function of the CP flow rate for the  
27 three chips modeled in this study. It can be easily seen that the dispensing rate increases  
28 as the CP flow rate increases (*i.e.* it increases from 3.6 drops $\cdot\text{s}^{-1}$  to 6.6 drops $\cdot\text{s}^{-1}$  as the CP  
29 flow rate increases from 100 to 500  $\mu\text{L}\cdot\text{h}^{-1}$  for the 25  $\mu\text{m}$  deep chip). By comparing the  
30 three chip designs, the greatest dispensing rate is obtained for the shallowest channel. In  
31 fact, the dispensing rate obtained for the deepest channel is approximately 55% smaller  
32 than the value reported for the shallowest channel for CP flow rates larger than 100  $\mu\text{L}\cdot\text{h}^{-1}$ .  
33 This is attributed to the relatively high velocity magnitudes achieved inside the 25  $\mu\text{m}$   
34 deep channel under the same conditions. These high velocities for the 25  $\mu\text{m}$  deep chip  
35 are translated into small droplet sizes and high dispensing rates, especially for high CP  
36 flow rates, as can be seen in Figures 5 a) and b).  
37  
38  
39  
40  
41  
42  
43  
44  
45  
46  
47  
48  
49  
50

51 Finally, in Figure 5 c) the experimental droplet size as a function of the CP flow rate is  
52 presented. It should be noted that the experimental chip has a U-shaped cross section,  
53 with a maximum depth of 30  $\mu\text{m}$ . However, the simulations assumed rectangular cross-  
54 section chip designs. Therefore, the experimental droplet sizes were compared with the  
55  
56  
57  
58  
59  
60

simulated data obtained with the 25  $\mu\text{m}$  deep channel as this design has a more similar cross-sectional area (the difference in the reported areas is around 8%). As seen in the figure, the experimental droplet size follows the same trend, with droplet sizes between 136.5  $\mu\text{m}$  and 242.6  $\mu\text{m}$  depending on the CP flow rate value. For the same range, the simulated size increases from 133.3  $\mu\text{m}$  to 233.2  $\mu\text{m}$ . Thus, the model results are in good agreement with the experimental data, with an average error of 4% for the CP flow rate range under study. Once the droplet generation simulations were analyzed, and the model was contrasted against experimental data, finding good agreement between the theoretical and experimental drop diameters, droplet deflection studies inside the multi-laminar flow chamber are evaluated.

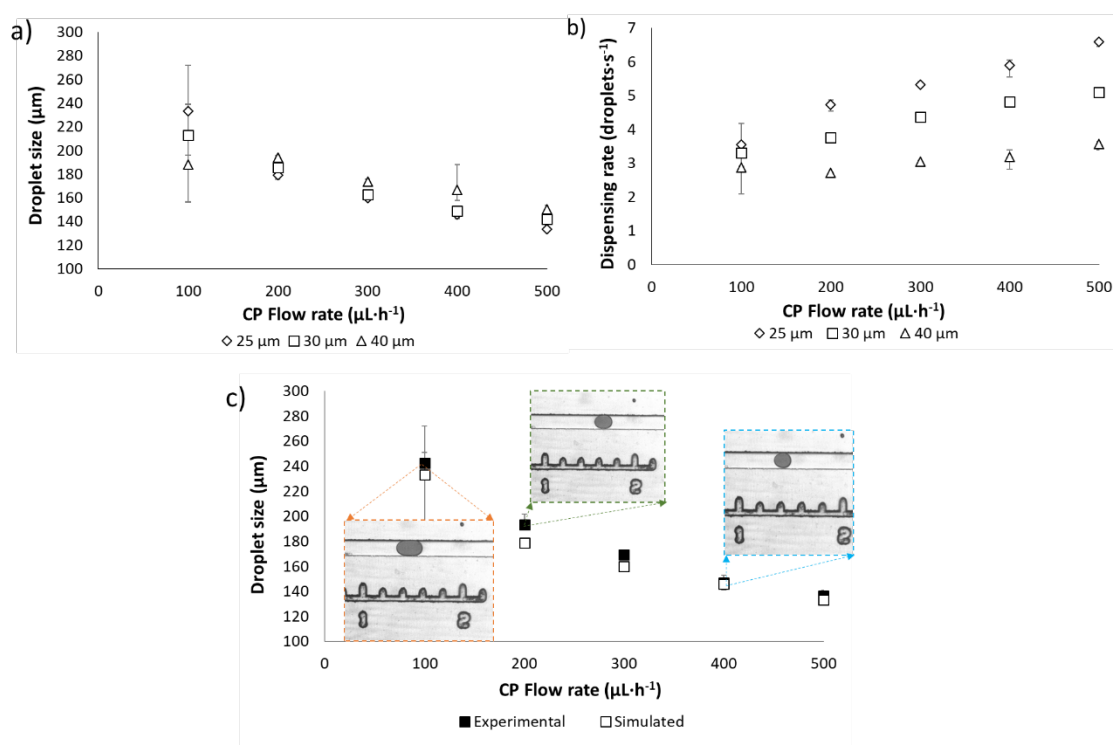


Figure 5. Simulation results for the flow-focusing droplet generation device (DP flow rate is fixed at  $10 \mu\text{L}\cdot\text{h}^{-1}$ ). a) Influence of the CP flow rate on the droplet size. b) Dispensing rate (i.e. number of droplets generated per second) as a function of the CP flow rate. c) Comparison between the experimental and the theoretical droplet diameter obtained with the droplet generation model.

## 4.2. Droplet deflection

In this section, droplet deflection through multi-laminar flow streams is evaluated as a function of the magnetic and fluidic drag forces experienced by the ferrofluid drops. It should be noted that for this study only the reaction chamber is modeled (*i.e.* the fluid domain consisted of a volume of  $8 \times 4.1 \times 0.1 \text{ mm}^3$ ). Thus, droplets are assumed to enter the domain at a constant size and dispensing rate and their trajectories are calculated as a function of the magnet position and the flow rates inside the chamber. As mentioned above, four magnet positions were tested in this study. In order to correctly analyze and understand droplet deflection results, both the magnetic field provided by the magnet inside the chamber and the corresponding force exerted on the droplets were first modeled. These studies are important in order to perform a quantitative analysis of the magnetic conditions provided by the four magnet locations.

In Figure 6 a) the magnetic field and force field distributions inside the reaction chamber are presented for the magnet position 1. The magnetic field ranges from 1 mT to 4 mT, and the force from 0.2 nN to 2.2 nN (in the negative y direction), reaching the highest field and force values at the bottom wall. For this position, the magnet is centered with respect to the x axis, and therefore, the highest force is obtained at  $x=0$ . Thus, droplets are expected to travel in the negative y direction, being attracted towards the lower wall if the magnetic force is not balanced with the fluidic drag force. In order to increase the magnetic field and force towards the chamber outlets, other positions with the magnet placed off-centered were tested (positions 2, 3 and 4, corresponding to Figures 6 b), c) and d), respectively). For these cases, the magnetic field and force distributions change significantly. Although the magnitudes of the magnetic fields and forces are similar for positions 2 and 4 (and these are similar to the ones observed for position 1), the highest force region is not located at  $x=0$  but at  $x=4 \text{ mm}$  (chamber lower outlet). Among the three

1  
2  
3 positions, the highest magnetic force is reached for the position number 3, with forces  
4  
5 ranging between 10 nN and 60 nN. These high magnetic forces are due to the distance  $d_1$   
6  
7 for this position, which is 0, *i.e.* the magnet is placed at the bottom of the outlets.  
8  
9  
10  
11  
12  
13  
14  
15  
16  
17  
18  
19  
20  
21  
22  
23  
24  
25  
26  
27  
28  
29  
30  
31  
32  
33  
34  
35  
36  
37  
38  
39  
40  
41  
42  
43  
44  
45  
46  
47  
48  
49  
50  
51  
52  
53  
54  
55  
56  
57  
58  
59  
60

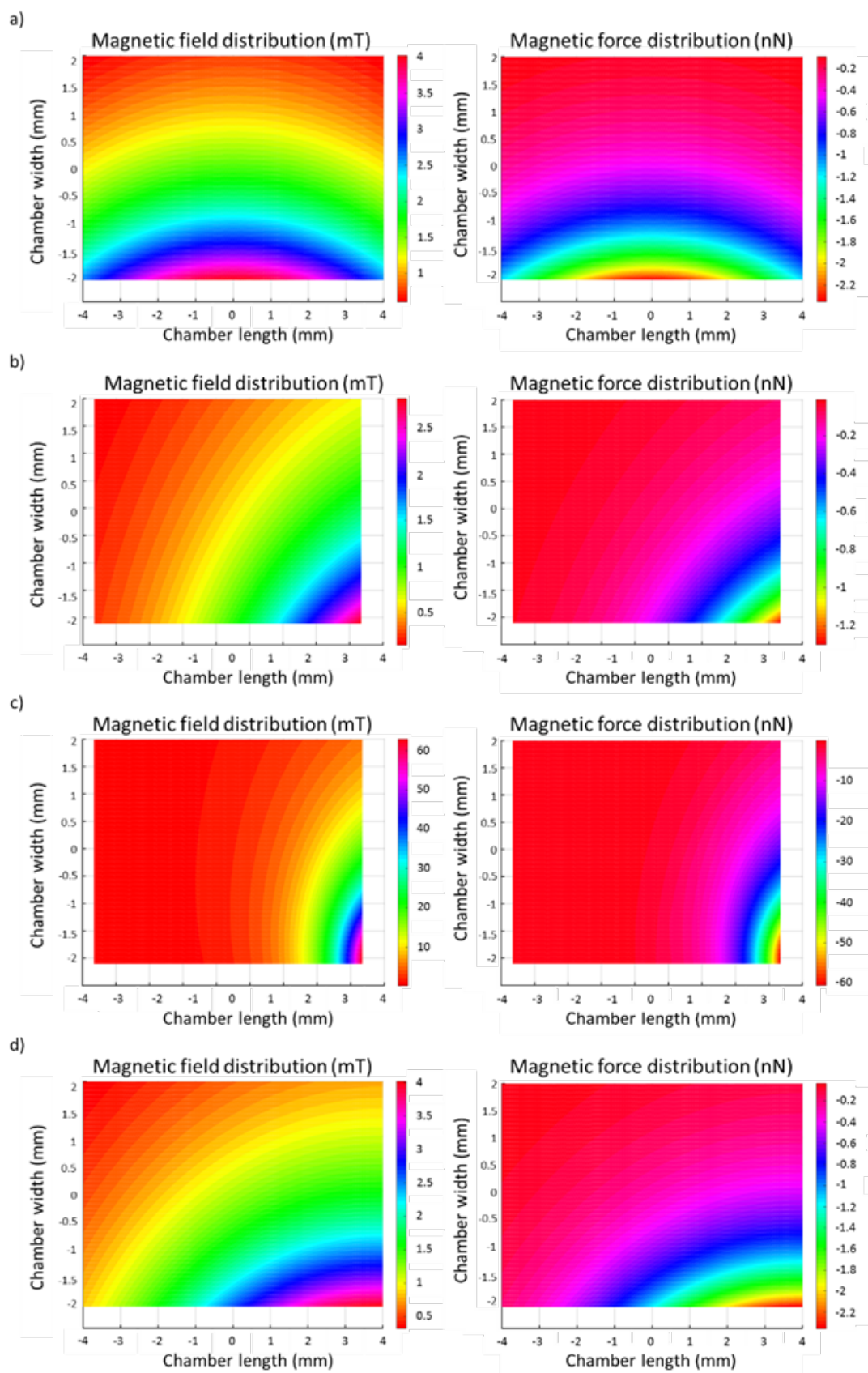


Figure 6. Magnetic field (left) and force (right) distributions inside the chamber for different magnet positions. Positions: a) 1; b) 2; c) 3; d) 4.

1  
2  
3 Once the magnetic conditions inside the chamber have been evaluated through the  
4 magnetic field and force analysis, droplet trajectories are experimentally and theoretically  
5 analyzed for the four magnet positions. For this analysis, the flow rates of the ink streams,  
6 CP and DP were kept at 300, 300, and 10  $\mu\text{L}\cdot\text{h}^{-1}$ , respectively. For these flow rates, the  
7 droplet diameter reaches 50  $\mu\text{m}$  and the dispensing rate was experimentally observed to  
8 be around 20 droplets $\cdot\text{s}^{-1}$ , which were employed as a simulation input parameter.  
9

10  
11 Before studying droplet deflection, it is useful to observe the system behavior when no  
12 magnetic field is applied. The experimental droplet generation and transport inside the  
13 chamber when no magnetic force is exerted on the templates is presented in Figure 7. In  
14 Figure 7 a) the experimental droplet generation is shown, followed by the droplet  
15 transport in the serpentine channel (Figure 7 b)) and the trajectory inside the chamber  
16 (Figure 7 c)). As seen in the figure, droplets are formed at the generation device that is 20  
17  $\mu\text{m}$  deep, and then, they are introduced inside the 100  $\mu\text{m}$  deep bottom channel that has  
18 the serpentine and the reaction chamber. At the generation device, droplets have a  
19 cylindrical shape but when they are injected into the deeper channel, they acquire  
20 spherical shapes. Then, they are transported along the serpentine and finally, they are  
21 introduced into the chamber. When there is no magnetic field externally applied, droplets  
22 are directed towards the outlet within the CP phase, as there is no magnetic force but only  
23 fluidic drag force, i.e. they follow the fluid streamlines from the inlet to the outlet. In this  
24 figure, the white and grey streams are the experimental blue and red inks, which are  
25 visualized with these colors with the monochrome, high-resolution CCD camera. In  
26 Figure 7 d), the theoretical trajectory followed by the droplets within the chamber for the  
27 same flowing conditions is presented. In this figure, the black points represent the  
28 droplets, the white and grey streams represent the experimental blue and red ink streams  
29 (modeled as scalar solutes), and the dark blue lines represent the fluid streamlines. As  
30  
31  
32  
33  
34  
35  
36  
37  
38  
39  
40  
41  
42  
43  
44  
45  
46  
47  
48  
49  
50  
51  
52  
53  
54  
55  
56  
57  
58  
59  
60

occurs experimentally, the simulation result shows that droplets are guided through the chamber following a straight line from the inlet to the outlet.

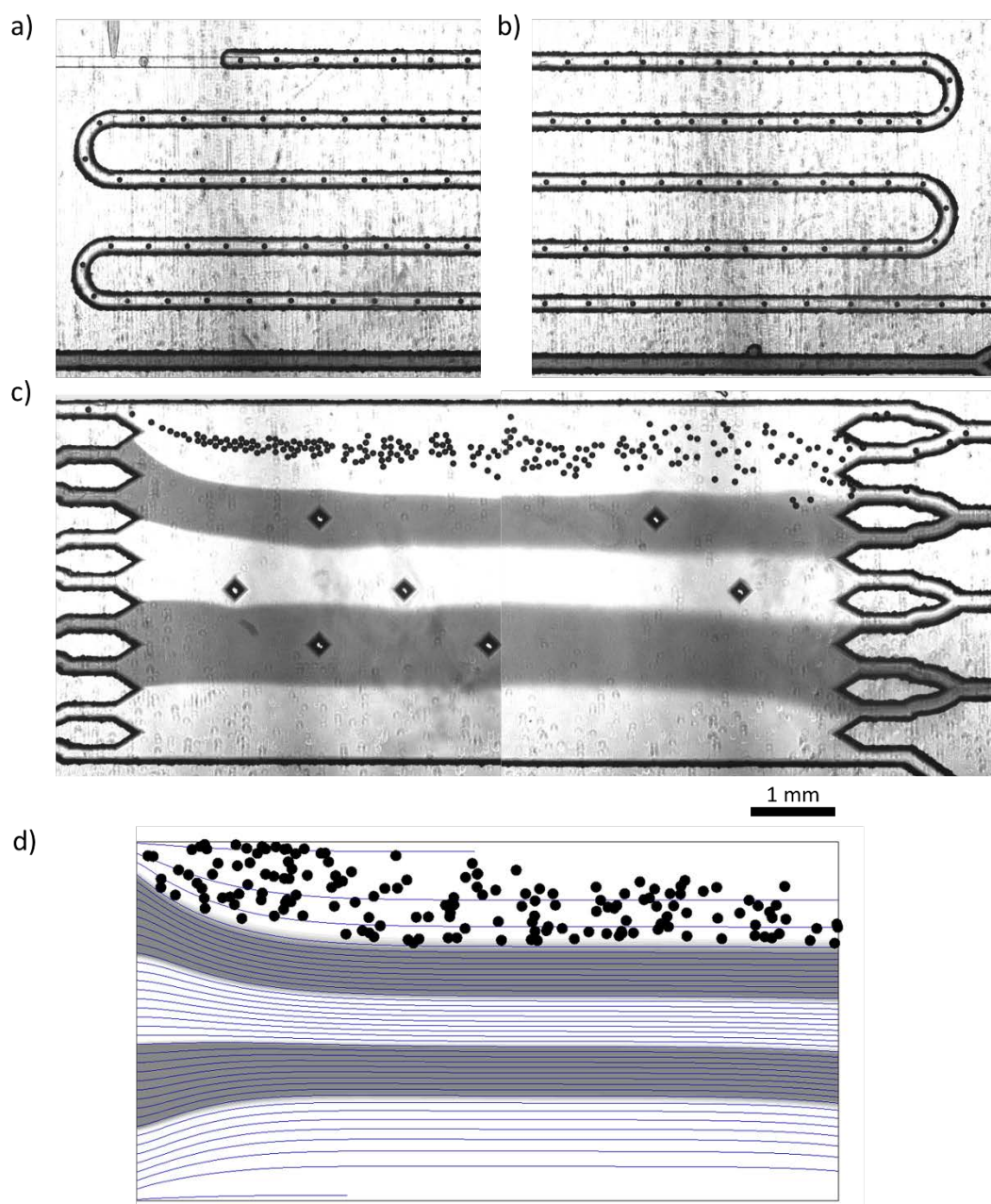


Figure 7. Droplet generation and transport inside the chamber without the influence of magnetic fields. a) Experimental droplet generation. b) Droplet transport along the serpentine that connects the generation region with the chamber. c) Experimental and d) theoretical droplet trajectories inside the chamber when no magnetic field is applied.

1  
2  
3 When the ferrofluid droplets are subjected to the influence of non-homogeneous magnetic  
4 fields, their trajectories vary inside the chamber. In Figures 8 a1) and a2) the theoretical  
5 and experimental droplet transport when the magnet is located at the position number 1  
6 are presented. For this magnetic condition, the highest force is located at the bottom wall  
7 around  $x=0$  as analyzed above (Figure 6 a)). Under this magnetic condition, droplets are  
8 slowly deflected across the streams, reaching the lower wall at  $x$  locations between 0 and  
9 2 mm for both the experimental and the theoretical results. In this case, the fluidic drag  
10 force is around 0.39 nN, which is smaller than the magnetic force due to the magnet. Once  
11 the droplets reach the wall, the magnetic force exerted on them is very high (around 2.2  
12 nN), whereas the fluidic drag force goes down to almost zero due to the laminar flow  
13 regime, *i.e.* zero velocity values at walls. In fact, for this magnet position, the flow  
14 alterations caused by the buildup of layers of droplets at the wall change the flow patterns  
15 inside the chamber. As the droplets are accumulated at the wall, the last ink stream cannot  
16 flow along its path, and has to flow above the droplet layers. This affects the flow of the  
17 other fluid streams in the chamber as seen in Figure 8 a2).

18  
19  
20  
21  
22  
23  
24  
25  
26  
27  
28  
29  
30  
31  
32  
33  
34  
35  
36  
37  
38 On the other hand, moving the magnet to the position number 2 resulted in the incomplete  
39 deflection, as seen in Figures 8 b1) (simulation results) and b2) (experimental  
40 micrograph). For this condition, the magnetic force is low for most of the zones inside  
41 the chamber, and only at the outlet reaches relatively high values. Thus, droplets are  
42 slightly deflected through the chamber, but they are not affected by the high magnetic  
43 force until they reach the outlet region. At this point, although the magnetic force slightly  
44 increases (Figure 6 b)), the droplets do not have enough distance to modify their trajectory  
45 and they exit the chip within the first ink stream, as seen both in the simulations and the  
46 experiments ( $y \geq 0$  mm). Therefore, higher magnetic fields and forces are required to  
47 completely deflect the droplets through all the streams.  
48  
49  
50  
51  
52  
53  
54  
55  
56  
57  
58  
59  
60

1  
2  
3 By using higher magnetic fields and forces (obtained after moving the magnet to position  
4 3), all the droplets are completely deflected (Figures 8 c1) and c2)). As seen in the  
5  
6 experimental micrograph, the high magnetic fields inside the chamber cause the  
7  
8 interaction between the droplets (*i.e.* magnetic coupling) and the high perturbation of the  
9  
10 flow field. These high magnetic fields and forces are not desirable for the continuous-  
11  
12 flow droplet processing due to several reasons. On the one hand, they cause the droplet-  
13  
14 droplet interactions mentioned above, which minimize the available droplet surface area  
15  
16 exposed to the fluids as they are aggregated, rendering a lower efficiency. On the other  
17  
18 hand, the high magnetic forces experienced by the droplets for this magnet position  
19  
20 (higher than 30 nN) cause strong fluid-droplet interactions as seen in the figures. For this  
21  
22 magnetic force field, droplets are not only aggregated but also highly accelerated towards  
23  
24 the outlet, which greatly perturbs the flow field, as shown in Figure 8 c1) where the  
25  
26 fluid streamlines are presented. This is not beneficial, as the droplets are not in contact  
27  
28 with the laminar flow streams in a homogeneous manner. In fact, the high magnetic force  
29  
30 exerted on the droplets causes the change of the flow patterns over time, depending on  
31  
32 the droplet position inside the channel. Thus, although droplet-droplet interactions are not  
33  
34 included in the model, the Lagrangian approach employed for modeling droplet deflection  
35  
36 is able to predict the magnetic field conditions that highly perturbate the flow field due to  
37  
38 the inclusion of a two-way coupling model.  
39  
40  
41  
42  
43  
44  
45

46 Finally, an optimization of the magnetic force necessary to deflect the droplets without  
47  
48 causing droplet aggregation nor high acceleration was carried out until the correct magnet  
49  
50 position was found. This magnet position is the number 4, which causes not only the  
51  
52 complete deflection of the ferrofluid droplets through all the streams, but also their  
53  
54 homogeneous transport avoiding extreme accelerations, as presented in Figures 8 d1) and  
55  
56 d2). For this magnet position, the magnetic force exerted on the material is between 1 nN  
57  
58  
59  
60

and 2 nN. As seen in the figures, the droplets reach the lower wall at x coordinates higher than 2 mm, and then, they are slowly directed towards the outlet.

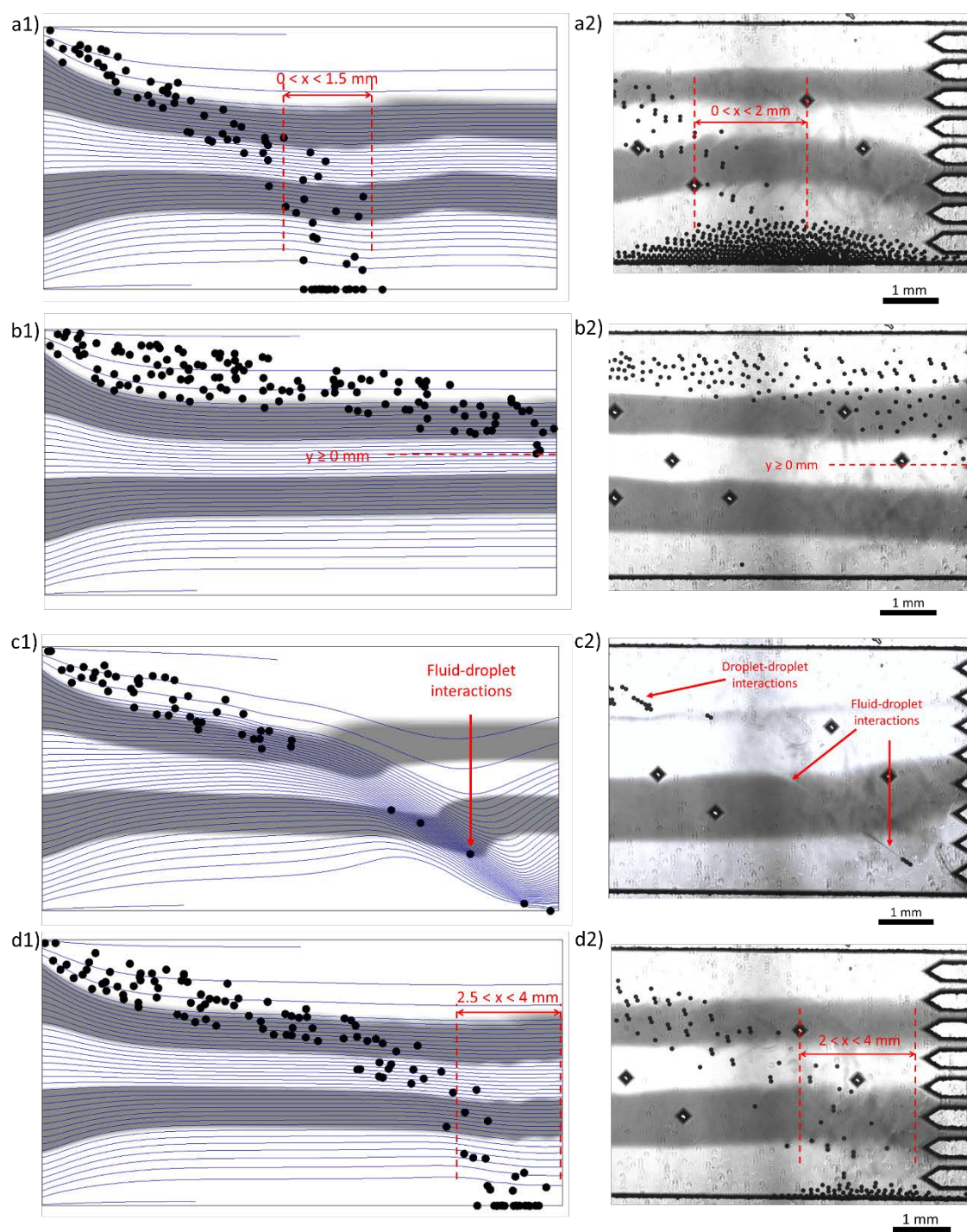
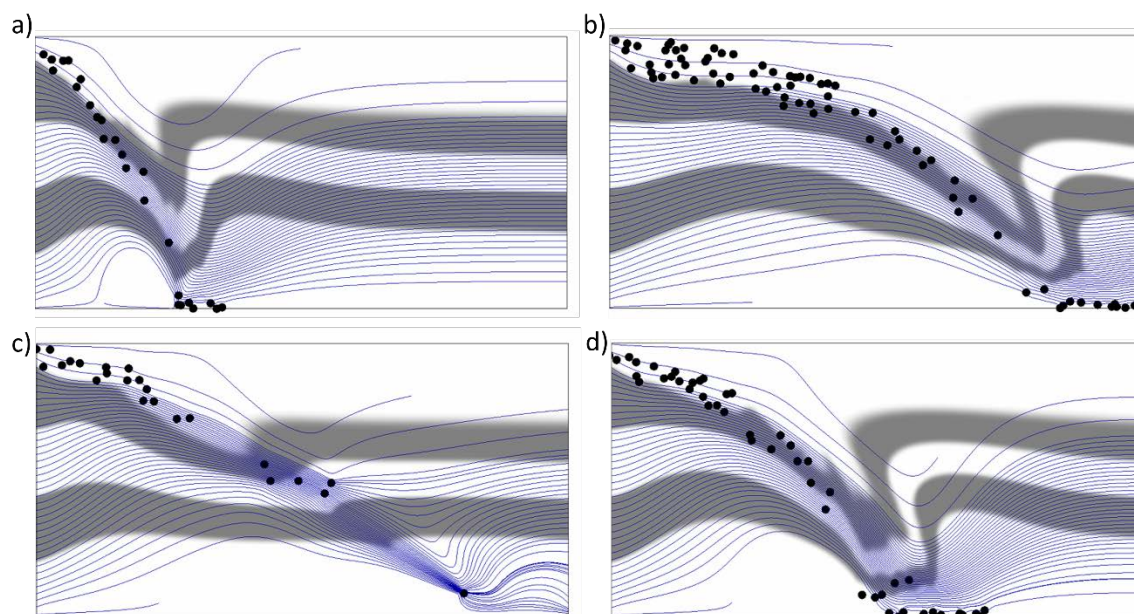


Figure 8. Trajectory of 50  $\mu\text{m}$  droplets under the influence of magnetic fields provided by the magnet located at position: a) 1; b) 2; c) 3; d) 4. On the left side the theoretical trajectory is presented whereas the experimental micrograph is shown on the right side.

1  
2  
3 It should be noted that the optimized magnet position depends on the droplet size and the  
4 flow field conditions. For example, we have simulated the trajectories of 100  $\mu\text{m}$  droplets  
5 for the same 4 magnet positions and flow rates. These results are presented in Figure 9.  
6  
7 Since the magnetic force is proportional to the volume of the droplet, and the drag force  
8 is proportional to the droplet radius ( $r$ ), the magnetophoretic mobility of larger droplets  
9 is higher (approximately proportional to  $r^2$ ).<sup>46</sup> This issue can be observed in the figure.  
10  
11 For positions 1 (Figure 9 a)) and 4 (Figure 9 d)), the droplets cross all the streams and  
12 reach the lower wall approximately at the center of the chamber. For positions 2 (Figure  
13 9 b)) and 3 (Figure 9 c)), the droplets travel fast from the inlet to the lower outlet, at a  
14 higher velocity than the one observed for 50  $\mu\text{m}$  droplets. Also, the perturbation of the  
15 flow is much more pronounced, as seen in all the figures. Thus, larger droplets have a  
16 larger magnetic mobility, resulting not only in the complete deflection but also in the  
17 severe perturbation of the laminar flow when the same magnet positions and flow rates  
18 are used.



56 Figure 9. Trajectory of 100  $\mu\text{m}$  droplets under the influence of magnetic fields provided  
57 by the magnet located at position: a) 1; b) 2; c) 3; d) 4.  
58  
59  
60

1  
2  
3 Continuing with the analysis of our base case, where 50  $\mu\text{m}$  droplets are modeled, it can  
4  
5 be seen that there exists high variability in the trajectories experienced by different  
6  
7 droplets for our optimized magnet position. The maximum difference in the trajectories  
8  
9 is around 2 mm in the x direction as seen in Figure 8 d). Therefore, the influence of the  
10  
11 flow rates on the trajectories of 50  $\mu\text{m}$  droplets is analyzed next. For this analysis, the  
12  
13 magnet location was kept constant at position 4.  
14  
15

16  
17 The influence of the flow rates on droplet transport was carried out by varying the flow  
18  
19 rates of the ink streams, of the CP and the DP. By increasing the flow rate of the ink  
20  
21 streams from 300  $\mu\text{L}\cdot\text{h}^{-1}$  to 600  $\mu\text{L}\cdot\text{h}^{-1}$ , and by decreasing the DP flow rate from 10  $\mu\text{L}\cdot\text{h}^{-1}$   
22  
23  $^1$  to 1  $\mu\text{L}\cdot\text{h}^{-1}$  (keeping the CP at 300  $\mu\text{L}\cdot\text{h}^{-1}$ ), homogeneous droplet trajectories were  
24  
25 obtained, as presented in Figures 10 a1) (simulation results) and a2) (experimental  
26  
27 micrograph). However, for these flowing conditions, complete deflection was not  
28  
29 achieved because the average drag force increases up to almost 0.8 nN. Therefore, it was  
30  
31 found that the optimum flow rates for the ink streams should be around 300  $\mu\text{L}\cdot\text{h}^{-1}$  as  
32  
33 presented before for the magnetic analysis. Nonetheless, the dispensing rate was reduced  
34  
35 to around 4 or 5 droplets $\cdot\text{s}^{-1}$  for this DP flow rate, which appears to benefit the  
36  
37 homogeneous trajectory of the droplets along the chamber. Therefore, the DP flow rate  
38  
39 was kept at 1  $\mu\text{L}\cdot\text{h}^{-1}$  for analyzing the influence of the CP flow rate.  
40  
41  
42

43  
44 Finally, the influence of the CP flow rate was studied by using two flow rates: 150  $\mu\text{L}\cdot\text{h}^{-1}$   
45  
46  $^1$  and 300  $\mu\text{L}\cdot\text{h}^{-1}$ . In Figure 10 b1) the simulated droplet trajectory is presented for a flow  
47  
48 rate value of the CP equal to 300  $\mu\text{L}\cdot\text{h}^{-1}$ . As it can be seen in the figure, droplets follow a  
49  
50 parabolic trajectory along the chamber, crossing all the streams, and reaching the wall at  
51  
52  $x \approx 2.5$  mm. This trajectory is in agreement with the path experimentally observed (Figure  
53  
54 10 b2)). This condition can be considered optimum as the droplets are individually guided  
55  
56 through all the streams and the trajectory followed by them is identical. For these  
57  
58  
59  
60

1  
2  
3 conditions, there is no variation between droplet trajectories as happens when the DP flow  
4 rate is ten times higher. However, due to the difference in the diameter of the inlets, a  
5 better optimization of the flow rates inside the chamber could be carried out to obtain the  
6 parallel co-flow of all the streams.<sup>47</sup> Thus, the CP flow rate was reduced to half (i.e. 150  
7  $\mu\text{L}\cdot\text{h}^{-1}$ ) in order to keep a better flow patterns within the chamber. The results after this  
8 optimization process are shown in Figure 10 c1) and c2). For this study, the optimum  
9 conditions to achieve droplet deflection, perfect flow patterns, and to avoid both droplet-  
10 droplet and droplet-fluid interactions are: magnet position 4, DP, CP and ink streams flow  
11 rates equal to 1  $\mu\text{L}\cdot\text{h}^{-1}$ , 150  $\mu\text{L}\cdot\text{h}^{-1}$  and 300  $\mu\text{L}\cdot\text{h}^{-1}$ , respectively. Although for these  
12 magnetic and fluidic conditions the theoretical droplet trajectory (Figure 10 c1)) is  
13 identical to the experimental one (Figure 10 c2)), the simulation results regarding the flow  
14 patterns slightly improve in comparison with the previous CP flow rate. However, the  
15 experimental data reveal the perfect parallel flow of all the streams within the chamber.  
16 In fact, the experimental micrograph shows both good deflection and perfect flow patterns  
17 with all the streams flowing in parallel. The difference between the experimental and the  
18 simulated results might be due to the influence of the inlet/outlet shapes, which were not  
19 included in the model in order to simplify the problem. Also, the columns inside the  
20 chamber (*i.e.* the 7 rhombohedral pillars that appear in the experimental micrograph,  
21 which were included in the chamber to provide mechanical stability) are not modeled,  
22 and their presence might affect the velocity field. Nonetheless, the observed and predicted  
23 results perfectly match for all the conditions tested in this study (with a difference  
24 between the theoretical and experimental droplet position of less than  $\pm 1$  mm inside the  
25  $8 \times 4.1$  mm<sup>2</sup> chamber), which validates the model for studying complex, LOC droplet-  
26 based applications.  
27  
28  
29  
30  
31  
32  
33  
34  
35  
36  
37  
38  
39  
40  
41  
42  
43  
44  
45  
46  
47  
48  
49  
50  
51  
52  
53  
54  
55  
56  
57  
58  
59  
60

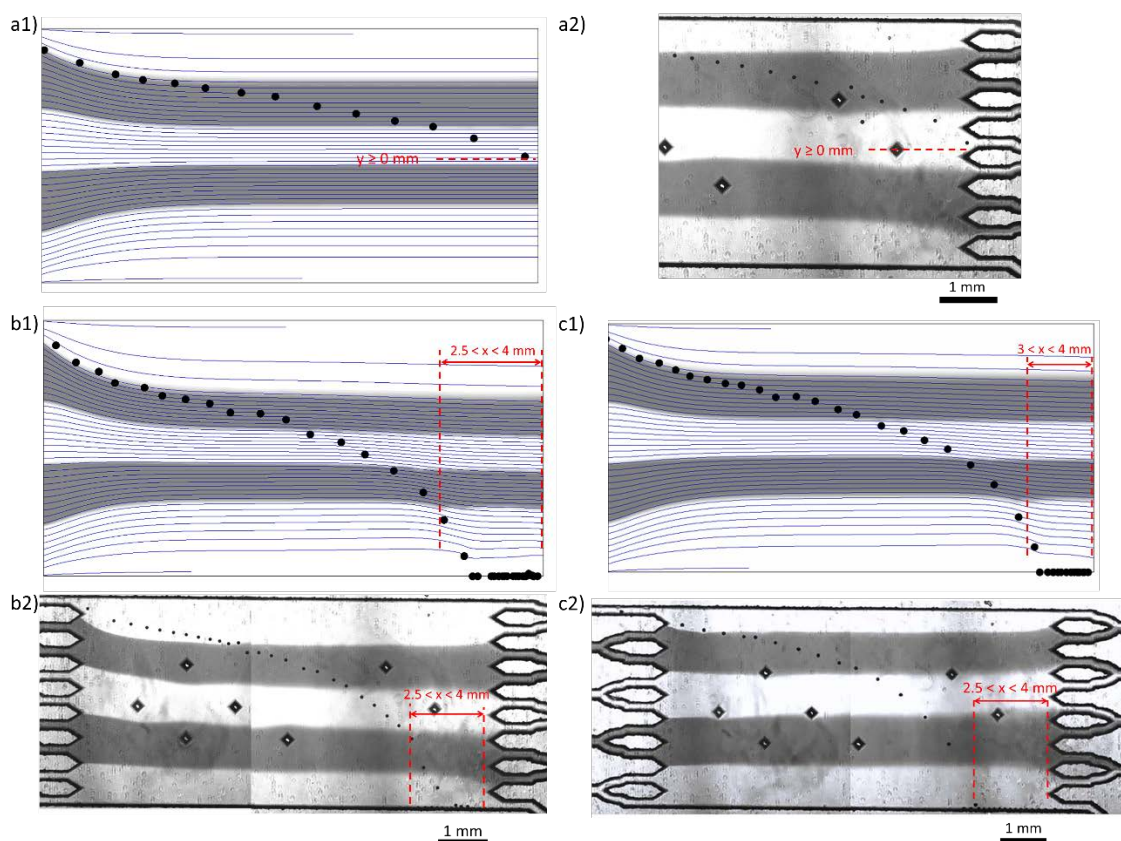


Figure 10. a1) Theoretical and a2) Experimental droplet trajectory for DP and ink streams flow rates equal to  $1 \mu\text{L}\cdot\text{h}^{-1}$  and  $600 \mu\text{L}\cdot\text{h}^{-1}$ , respectively. b1) Theoretical and b2) Experimental droplet trajectory for DP, CP and ink streams flow rates equal to  $1 \mu\text{L}\cdot\text{h}^{-1}$ ,  $300 \mu\text{L}\cdot\text{h}^{-1}$  and  $300 \mu\text{L}\cdot\text{h}^{-1}$ , respectively. c1) Theoretical and c2) Experimental device performance when the optimum conditions are employed (magnet position 4, DP, CP and ink streams flow rates equal to  $1 \mu\text{L}\cdot\text{h}^{-1}$ ,  $150 \mu\text{L}\cdot\text{h}^{-1}$  and  $300 \mu\text{L}\cdot\text{h}^{-1}$ , respectively).

## 5. CONCLUSIONS

In this article, a 2-step CFD approach was implemented to investigate the dynamic behavior of ferrofluid droplets for continuous-flow droplet-based microfluidic processes. The developed approach predicts both ferrofluid droplet generation and magnetic deflection across multi-laminar flow streams. Different variables and parameters were

1  
2  
3 analyzed, both theoretically and experimentally, in order to optimize the device  
4 performance for its application to the continuous-flow droplet processing.  
5  
6

7 Firstly, droplet generation was studied at a flow-focusing generation device. The  
8 theoretical model includes an Eulerian CFD approach, where the surface tension  
9 contributions are modeled. For this stage, the influence of the flow rates and the device  
10 dimensions on both droplet size and dispensing rate was investigated. The results show  
11 that although the droplet diameter slightly varies with the flow rates and the chip depth,  
12 the dispensing rate is highly affected when these conditions vary. Furthermore, the  
13 validation of the model was carried out as the theoretical predictions were found to be in  
14 good agreement with the experimental observations.  
15  
16

17 In the second stage, droplet transport across a millimeter reaction chamber with 5 parallel  
18 streams under the influence of non-homogeneous magnetic fields was optimized. The  
19 theoretical model used to describe droplet deflection includes an Eulerian-Lagrangian  
20 approach, with droplets treated as point-like particles. Different magnet positions and  
21 flow rates were investigated. The simulated results were compared against experimental  
22 data, and the results indicated that droplet trajectory, flow patterns and droplet-fluid  
23 interactions inside the chamber were in good agreement with the model predictions.  
24 Therefore, a full modeling approach including surface tension contributions can be  
25 avoided when modeling droplet deflection in relatively large lab-on-a-chip devices, thus  
26 improving computational efficiency.  
27  
28

29 It should be also noted that this is the first two-step computational approach reported for  
30 modeling droplets in big multi-laminar flow chambers and it should prove useful in the  
31 design of a high number of applications. The deflection of magnetic droplets across  
32 parallel streams containing different reagents can be exploited in multiple fields. In fact,  
33 this technique has been recently reported for the layer-by-layer coating of droplet  
34  
35  
36  
37  
38  
39  
40  
41  
42  
43  
44  
45  
46  
47  
48  
49  
50  
51  
52  
53  
54  
55  
56  
57  
58  
59  
60

1  
2  
3 templates with polyelectrolytes for the continuous-flow assembly of drug delivery  
4 capsules.<sup>35</sup> Furthermore, the use of multiple magnets sequentially placed on top and  
5  
6 bottom of the chamber allows the magnetic droplets to move back-and-forth through the  
7  
8 streams in a zig-zag motion, a technique that can be employed for performing bioassays.<sup>48</sup>  
9  
10  
11 Thus, we believe that this modeling approach can result very useful for the design of a  
12  
13 high number of lab-on-a-chip devices in advance of fabrication.  
14  
15  
16  
17  
18

## 19 ACKNOWLEDGEMENTS

20  
21 Financial support from the Spanish Ministry of Economy and Competitiveness under the  
22 projects CTQ2015-72364-EXP and CTQ2015-66078-R (MINECO/FEDER) is gratefully  
23 acknowledged. Jenifer Gómez-Pastora also thanks the FPI postgraduate research grant  
24 (BES-2013-064415). Edward P. Furlani gratefully acknowledges financial support from  
25  
26 the U.S. National Science Foundation, through Award CBET-1337860.  
27  
28  
29  
30  
31  
32  
33  
34

## 35 REFERENCES

- 36  
37 (1) Teh, S. Y.; Lin, R.; Hung L. H.; Lee, A. P. Droplet Microfluidics. *Lab Chip*, **2008**, *8*,  
38 198–220.  
39  
40  
41 (2) Serra, M.; Ferraro, D.; Pereiro, I.; Viovy, J. L.; Descroix, S. The Power of Solid  
42 Supports in Multiphase and Droplet-Based Microfluidics: Towards Clinical  
43 Applications. *Lab Chip*, **2017**, *17*, 3979–3999.  
44  
45  
46 (3) Zhang, Y.; Nguyen, N. T. Magnetic Digital Microfluidics – A Review. *Lab Chip*,  
47 **2017**, *17*, 994–1008.  
48  
49  
50 (4) Renaudin, A.; Sozanski, J. P.; Verbeke, B.; Zhang, V.; Tabourier, P.; Druon, C.  
51 Monitoring SAW-Actuated Microdroplets in View of Biological Applications. *Sens.*  
52 *Actuators, B*, **2009**, *138*, 374–382.  
53  
54  
55  
56  
57  
58  
59  
60

- 1  
2  
3 (5) Chong, Z. Z.; Tan, S. H.; Gañán-Calvo, A. M.; Tor, S. B.; Loh, N. H.; Nguyen, N. T.  
4  
5 Active Droplet Generation in Microfluidics. *Lab Chip*, **2016**, *16*, 35–58.  
6  
7  
8 (6) Pit, A. M.; Duits, M. H. G.; Mugele, F. Droplet Manipulations in Two Phase Flow  
9  
10 Microfluidics. *Micromachines*, **2015**, *6*, 1768–1793.  
11  
12  
13 (7) Huang, H.; Yu, Y.; Hu, Y.; He, X.; Usta, O. B.; Yarmush, M. L. Generation and  
14  
15 Manipulation of Hydrogel Microcapsules by Droplet-Based Microfluidics for  
16  
17 Mammalian Cell Culture. *Lab Chip*, **2017**, *17*, 1913–1932.  
18  
19  
20 (8) Al-Hetlani, E.; Hatt, O. J.; Vojtíšek, M.; Tarn, M. D.; Iles, A.; Pamme, N. Sorting and  
21  
22 Manipulation of Magnetic Droplets in Continuous Flow. *AIP Conference*  
23  
24 *Proceedings*, **2010**, *1311*, 167–175.  
25  
26  
27 (9) Lombardi, D.; Dittrich, P. S. Droplet Microfluidics with Magnetic Beads: A New Tool  
28  
29 to Investigate Drug–Protein Interactions. *Anal. Bioanal. Chem.*, **2011**, *399*, 347–352.  
30  
31  
32 (10) Beyzavi, A.; Nguyen, N. T. Programmable Two-Dimensional Actuation of  
33  
34 Ferrofluid Droplet Using Planar Microcoils. *J. Micromech. Microeng.*, **2010**, *20*,  
35  
36 015018.  
37  
38  
39 (11) Pamme, N. Magnetism and Microfluidics. *Lab Chip*, **2006**, *6*, 24–38.  
40  
41  
42 (12) Huang, J. P.; Ge, X. H.; Xu, J. H.; Luo, G. S. Controlled Formation and Coalescence  
43  
44 of Paramagnetic Ionic Liquid Droplets under Magnetic Field in Coaxial Microfluidic  
45  
46 Devices. *Chem. Eng. Sci.*, **2016**, *152*, 293–300.  
47  
48  
49 (13) Mats, L.; Logue, F.; Oleschuk, R. D. “Particle-Free” Magnetic Actuation of Droplets  
50  
51 on Superhydrophobic Surfaces Using Dissolved Paramagnetic Salts. *Anal. Chem.*,  
52  
53 **2016**, *88*, 9486–9494.  
54  
55  
56 (14) Zhang, K.; Liang, Q.; Ai, X.; Hu, P.; Wang, Y.; Luo, G. On-Demand Microfluidic  
57  
58 Droplet Manipulation Using Hydrophobic Ferrofluid as a Continuous-Phase. *Lab*  
59  
60 *Chip*, **2011**, *11*, 1271–1275.

- 1  
2  
3 (15) Jamalabadi, M. Y. A.; DaqiqShirazi, M.; Kosar, A.; Shadloo, M. S. Effect of  
4 Injection Angle, Density Ratio, and Viscosity on Droplet Formation in a Microfluidic  
5 T-Junction. *Theor. Appl. Mech. Lett.*, **2017**, *7*, 243–251.  
6  
7  
8  
9  
10 (16) Sontti, S. G.; Atta, A. CFD Analysis of Microfluidic Droplet Formation in Non-  
11 Newtonian Liquid. *Chem. Eng. J.*, **2017**, *330*, 245–261.  
12  
13  
14 (17) Liu, J.; Tan, S. H.; Yap, Y. F.; Ng, M. Y.; Nguyen, N. T. Numerical and  
15 Experimental Investigations of the Formation Process of Ferrofluid Droplets.  
16 *Microfluid. Nanofluid.*, **2011**, *11*, 177–187.  
17  
18  
19  
20 (18) Sen, U.; Chatterjee, S.; Sen, S.; Tiwari, M. K.; Mukhopadhyay, A.; Ganguly, R.  
21 Dynamics of Magnetic Modulation of Ferrofluid Droplets for Digital Microfluidic  
22 Applications. *J. Magn. Magn. Mater.*, **2017**, *421*, 165–176.  
23  
24  
25  
26 (19) Aboutalebi, M.; Bijarchi, M. A.; Shafii, M. B.; Hannani, S. K. Numerical  
27 Investigation on Splitting of Ferrofluid Microdroplets in T-Junctions Using an  
28 Asymmetric Magnetic Field with Proposed Correlation. *J. Magn. Magn. Mater.*,  
29 **2018**, *447*, 139–149.  
30  
31  
32  
33 (20) Chakrabarty, D.; Dutta, S.; Chakraborty, N.; Ganguly, R. Magnetically Actuated  
34 Transport of Ferrofluid Droplets over Micro-Coil Array on a Digital Microfluidic  
35 Platform. *Sens. Actuators B Chem.*, **2016**, *236*, 367–377.  
36  
37  
38  
39 (21) Lohrasebi, A. Computational Modeling of the Effect of an External Magnetic Field  
40 on a Ferromagnetic Fluid Droplet. *J. Supercond. Nov. Magn.*, **2015**, *28*, 777–780.  
41  
42  
43  
44 (22) Grant, H.; Scardovelli, R.; Trubatch, A. D.; Yecko, P. A. Height Function Based  
45 Volume of Fluid Code for Simulations of Multiphase Magnetic Fluids. *Comput.*  
46 *Fluids*, **2015**, *113*, 112–118.  
47  
48  
49  
50 (23) Habera, M.; Hron, J. Modelling of a Free-Surface Ferrofluid Flow. *J. Magn. Magn.*  
51 *Mater.*, **2017**, *431*, 157–160.  
52  
53  
54  
55  
56  
57  
58  
59  
60

- 1  
2  
3 (24) Afkhami, S.; Tyler, A. J.; Renardy, Y.; Renardy, M.; St. Pierre, T. G.; Woodward,  
4 R. C.; Riffle, J. S. Deformation of a Hydrophobic Ferrofluid Droplet Suspended in a  
5 Viscous Medium under Uniform Magnetic Fields. *J. Fluid Mech.*, **2010**, *663*, 358–  
6 384.  
7  
8  
9  
10  
11  
12 (25) Zhu, G. P.; Nguyen, N. T.; Ramanujan, R. V.; Huang, X. Y. Nonlinear Deformation  
13 of a Ferrofluid Droplet in a Uniform Magnetic Field. *Langmuir*, **2011**, *27*, 14834–  
14 14841.  
15  
16  
17  
18  
19 (26) Rowghanian, P.; Meinhart, C. D.; Campas, O. Dynamics of Ferrofluid Drop  
20 Deformations under Spatially Uniform Magnetic Fields. *J. Fluid Mech.*, **2016**, *802*,  
21 245–262.  
22  
23  
24  
25  
26 (27) Beyzavi, A.; Nguyen, N. T. One-Dimensional Actuation of a Ferrofluid Droplet by  
27 Planar Microcoils. *J. Phys. D: Appl. Phys.*, **2009**, *42*, 015004.  
28  
29  
30  
31 (28) Shi, D.; Bi, Q.; Zhou, R. Numerical Simulation of a Falling Ferrofluid Droplet in a  
32 Uniform Magnetic Field by the VOSET Method. *Numer. Heat Tr. A Appl.*, **2014**, *66*,  
33 144–164.  
34  
35  
36  
37  
38 (29) Cimbala, R.; Kurimsky, J.; Rajnak, M.; Paulovicova, K.; Timko, M.; Kopcansky, P.;  
39 Kolcun, M.; Kosterec, M.; Bucko, S.; Kurimska, M. Magnetic Fluid Droplet  
40 Deformation in Electrostatic Field. *J. Electrostat.*, **2017**, *88*, 55–59.  
41  
42  
43  
44  
45 (30) Jackson, B. A.; Terhune, K. J.; King, L. B. Ionic Liquid Ferrofluid Interface  
46 Deformation and Spray Onset under Electric and Magnetic Stresses. *Phys. Fluids*,  
47 **2017**, *29*, 064105.  
48  
49  
50  
51 (31) Ghaffari, A.; Hashemabadi, S. H.; Bazmi, M. CFD Simulation of Equilibrium Shape  
52 and Coalescence of Ferrofluid Droplets Subjected to Uniform Magnetic Field.  
53 *Colloids Surf. A*, **2015**, *481*, 186–198.  
54  
55  
56  
57  
58  
59  
60

- 1  
2  
3 (32) Kadivar, E. Magnetocoalescence of Ferrofluid Droplets in a Flat Microfluidic  
4 Channel. *EPL*, **2014**, *106*, 24003.  
5  
6  
7  
8 (33) Ray, A.; Varma, V. B.; Jayaneel, P. J.; Sudharsan, N. M.; Wang, Z. P.; Ramanujan,  
9 R. V. On Demand Manipulation of Ferrofluid Droplets by Magnetic Fields. *Sens.*  
10 *Actuators B Chem.*, **2017**, *242*, 760–768.  
11  
12  
13  
14 (34) Varma, V. B.; Ray, A.; Wang, Z. M.; Wang, Z. P.; Ramanujan, R. V. Droplet  
15 Merging on a Lab-on-a-Chip Platform by Uniform Magnetic Fields. *Sci. Rep.*, **2016**,  
16 *6*, 37671.  
17  
18  
19  
20  
21 (35) Alorabi, A. Q.; Tarn, M. D.; Gomez-Pastora, J.; Bringas, E.; Ortiz, I.; Paunov, V.  
22 N.; Pamme, N. On-Chip Polyelectrolyte Coating onto Magnetic Droplets – Towards  
23 Continuous Flow Assembly of Drug Delivery Capsules. *Lab Chip*, **2017**, *17*,  
24 3785–3795.  
25  
26  
27  
28  
29  
30  
31 (36) Korlie, M. S.; Mukherjee, A.; Nita, B. G.; Stevens, J. G.; Trubatch, A. D.; Yecko, P.  
32 Modeling Bubbles and Droplets in Magnetic Fluids. *J. Phys.: Condens. Matter*, **2008**,  
33 *20*, 204143.  
34  
35  
36  
37  
38 (37) Scardovelli, R.; Zaleski, S. Direct Numerical Simulation of Free-Surface and  
39 Interfacial Flow. *Annu. Rev. Fluid Mech.*, **1999**, *31*, 567–603.  
40  
41  
42 (38) Hirt, C. W.; Nichols, B. D. Volume of Fluid (VOF) Method for the Dynamics of  
43 Free Boundaries. *J. Comput. Phys.*, **1981**, *39*, 201–225.  
44  
45  
46  
47 (39) Gomez-Pastora, J.; Karampelas, I. H.; Xue, X.; Bringas, E.; Furlani, E. P.; Ortiz, I.  
48 Magnetic Bead Separation from Flowing Blood in a Two-Phase Continuous-Flow  
49 Magnetophoretic Microdevice: Theoretical Analysis through Computational Fluid  
50 Dynamics Simulation. *J. Phys. Chem. C*, **2017**, *121*, 7466–7477.  
51  
52  
53  
54  
55  
56 (40) Gomez-Pastora, J.; Gonzalez-Fernandez, C.; Real, E.; Iles, A.; Bringas, E.; Furlani,  
57 E. P.; Ortiz, I. Computational Modeling and Fluorescence Microscopy  
58  
59  
60

- 1  
2  
3 Characterization of a Two-Phase Magnetophoretic Microsystem for Continuous-Flow  
4  
5 Blood Detoxification. *Lab Chip*, **2018**, *18*, 1593–1606.  
6  
7  
8 (41) Furlani, E. P.; Xue, X. A Model for Predicting Field-Directed Particle Transport in  
9  
10 the Magnetofection Process. *Pharm. Res.*, **2012**, *29*, 1366–1379.  
11  
12 (42) Khashan, S. A.; Furlani, E. P. Coupled Particle-Fluid Transport and Magnetic  
13  
14 Separation in Microfluidic Systems with Passive Magnetic Functionality. *J. Phys. D*  
15  
16 – *Appl. Phys.*, **2013**, *46*, 125002.  
17  
18  
19 (43) Furlani, E. P. *Permanent Magnet and Electromechanical Devices; Materials,*  
20  
21 *Analysis and Applications*; Academic Press: New York, 2001.  
22  
23  
24 (44) Wakaba, L.; Balachandar, S. On the Added Mass Force at Finite Reynolds and  
25  
26 Acceleration numbers. *Theor. Comput. Fluid Dyn.*, **2007**, *21*, 147–153.  
27  
28  
29 (45) Scheuble, N.; Iles, A.; Wootton, R. C. R.; Windhab, E. J.; Fischer, P.; Elvira, K. S.  
30  
31 Microfluidic Technique for the Simultaneous Quantification of Emulsion Instabilities  
32  
33 and Lipid Digestion Kinetics. *Anal. Chem.*, **2017**, *89*, 9116–9123.  
34  
35  
36 (46) Nguyen, N. T. Micro-Magnetofluidics: Interactions between Magnetism and Fluid  
37  
38 Flow on the Microscale. *Microfluid. Nanofluid.*, **2012**, *12*, 1–16.  
39  
40  
41 (47) Gomez-Pastora, J.; Gonzalez-Fernandez, C.; Fallanza, M.; Bringas, E.; Ortiz, I.  
42  
43 Flow Patterns and Mass Transfer Performance of Miscible Liquid-Liquid Flows in  
44  
45 Various Microchannels: Numerical and Experimental studies. *Chem. Eng. J.*, **2018**,  
46  
47 *344*, 487–497.  
48  
49  
50 (48) Gao, Y.; Lam, A. W. Y.; Chan, W. C. W. Automating Quantum Dot Barcode Assays  
51  
52 Using Microfluidics and Magnetism for the Development of a Point-of-Care Device.  
53  
54 *ACS Appl. Mater. Interfaces*, **2013**, *5*, 2853–2860.  
55  
56  
57  
58  
59  
60

### TOC GRAPHIC

